AMERICAN
METEOROLOGICAL
SOCIETY

Journal of Physical Oceanography

EARLY ONLINE RELEASE

This is a preliminary PDF of the author-produced manuscript that has been peer-reviewed and accepted for publication. Since it is being posted so soon after acceptance, it has not yet been copyedited, formatted, or processed by AMS Publications. This preliminary version of the manuscript may be downloaded, distributed, and cited, but please be aware that there will be visual differences and possibly some content differences between this version and the final published version.

The DOI for this manuscript is doi: 10.1175/2008JPO3961.1

The final published version of this manuscript will replace the preliminary version at the above DOI once it is available.

The effect of breaking waves on a coupled model of wind and ocean surface waves: I. Mature seas

Tobias Kukulka *†

Tetsu Hara

Graduate School of Oceanography, University of Rhode Island

Narragansett, RI 02882, USA

Submitted to Journal of Physical Oceanography (12/3/2007)

Revised 3/29/2008

*Corresponding author, email: kukulka@whoi.edu, phone: (508) 289-3455

†Now at Woods Hole Oceanographic Institution, Woods Hole, MA 02543, USA

Abstract

This is the first part of a two-part investigation of a coupled wind and wave model that includes the enhanced form drag of breaking waves. In part 1 the model is developed and applied to mature seas. Part 2 explores the solutions in a wide range of wind and wave conditions, including growing seas. Breaking and non-breaking waves induce air-side fluxes of momentum and energy above the air-sea interface. By balancing air-side momentum and energy and by conserving wave energy, coupled nonlinear advance-delay differential equations are derived, which govern simultaneously the wave and wind field. The system of equations is closed by introducing a relation between the wave height spectrum and wave dissipation due to breaking. The wave dissipation is proportional to nonlinear wave interactions, if the wave curvature spectrum is below the "threshold saturation level". Above this threshold the wave dissipation rapidly increases, so that the wave height spectrum is limited. The coupled model is applied for mature wind-driven seas for which the wind forcing only occurs in the equilibrium range away from the spectral peak. Modeled wave height curvature spectra as functions of wavenumber, k, are consistent with observations and transition from $k^{1/2}$ at low wavenumbers to k^0 at high wavenumbers. Breaking waves affect only weakly the wave height spectrum. Furthermore, the wind input to waves is dominated by non-breaking waves closer to the spectral peak. Shorter breaking waves, however, can support a significant fraction, which increases with wind speed, of the total air-sea momentum flux.

1 Introduction

Understanding the role of breaking surface waves in air-sea exchange processes is integral to improving parameterization schemes for coupled ocean-atmosphere models, which are commonly used for weather and climate predictions (*Komen et al.*, 1996). Although there exists evidence that wind-generated breaking surface waves enhance air-sea fluxes of heat, gases, and momentum, the mechanisms that lead to this enhancement are poorly understood (*Melville*, 1996). The need to incorporate the breaking wave effect more realistically in operational wave models is also highlighted in a recent review by *Cavaleri* (2006).

Previous laboratory experiments indicate that airflow separation at the lee of a breaking wave leads to an enhanced wave form drag compared to the form drag of non-breaking waves (*Banner*, 1990). Laboratory measurements have been obtained under well-controlled conditions for a monochromatic breaking wave. In the open ocean, however, breaking waves are randomly distributed and occur simultaneously over a wide range of scales (*Banner and Peregrine*, 1993). To quantify wave breaking for random seas, *Phillips* (1985) introduced the breaking wave distribution, which is the average length of breaking crests per unit sea surface area as a function of wave scale. Such a distribution was observed for oceanic field conditions by tracking white caps of breaking waves via aerial imaging analysis (*Melville and Matusov*, 2002).

This is part 1 of a two part study to investigate how a random distribution of breaking waves influences ocean surface wave spectra and the wind aloft. In part 1 we construct a coupled wind and wave model and apply the model to mature seas. Part 2 (*Kukulka and Hara*, 2007) examines the solutions in a wide range of wind and wave conditions, including growing seas.

1.1 Equilibrium range of wind waves

An important concept for modeling wind-waves is the equilibrium range of surface wave spectra, in which the wave field is nearly stationary, so that wave dissipation, energy re-

distribution due to nonlinear interactions, and the wind-input balance each other (*Phillips*, 1985). An upper limit of the equilibrium range was first found, assuming that the wave height is limited by wave breaking (*Phillips*, 1958). If the breaking process is independent of wind properties, this leads to the well known ω^{-5} power law of the wave height frequency spectrum ("frequency spectrum"), where ω is the angular frequency measured in SI units (or k^{-4} dependency of the wave height wavenumber spectrum ["wavenumber spectrum"], where k is the angular wavenumber measured in SI units). Observations, however, show a systematic deviation from such a power law for frequencies just above the peak frequency with a frequency dependence of ω^{-4} (*Jones and Toba*, 2001).

In analogy to Kolmogoroff's hypothesis for isotropic turbulence, the assumption that the energy flux through gravity waves in the equilibrium range is constant, yields the ω^{-4} power law (*Kitaigorodskii*, 1983). Later, the ω^{-4} power law was derived by assuming that dissipation, wind-input, and nonlinear interactions are all significant and proportional to each other (*Phillips*, 1985). In these two models, the wave field consists of a superposition of weakly nonlinear surface gravity waves with random phase.

In contrast, self-similar sharp crested breaking waves dominate the equilibrium range in the model by Belcher and Vassilicos (1997). Based on this assumption, the wave height spectrum must also be self-similar, in the sense that it follows a power law in some measure of wave scale (e.g., wavelength or phase speed). Imposing furthermore a dynamical balance between dissipation and nonlinear interactions results in a k^{-4} dependency of the wavenumber spectrum (*Belcher and Vassilicos*, 1997). The wind-wave equilibrium range models that we discussed so far, did not explicitly take into account that longer waves extract energy and momentum from the wind and thereby reduce the wind forcing on the shorter waves.

1.2 Wind and waves coupling

Under idealized conditions, the wind profile changes over time due to momentum and energy transfer from wind to waves, until the waves do not grow any more because the energy transfer is quenched (*Janssen*, 1982). Applying a quasi linear approximation to the governing

hydrodynamic equations results in a modification of the mean wind flow due to the presence of waves (*Janssen*, 1989; *Jenkins*, 1992, 1993). Using the nonlinear Reynolds equations for the air, wave-induced fluxes can be modeled in the boundary layer above waves, which is called the "wave boundary layer" (WBL) (*Chalikov and Makin*, 1991). The WBL is a thin layer within the constant stress layer where the wind stress partitions into the wave-induced stress and the turbulent stress (or the viscous stress inside the viscous sublayer). The effects of wave motion on the mean wind properties in the WBL can be investigated employing a wave following curvilinear coordinate system (*Jenkins*, 1992).

Hara and Belcher (2002) showed that the frequency spectrum transitions asymptotically from ω^{-4} to ω^{-5} at high frequencies, because shorter waves are forced by a reduced turbulent stress due to the momentum uptake of longer waves. The transition frequency, however, was inconsistent with observations.

Within the WBL, the mean wind speed profile can be determined, based on the energy balances of mean, wave-induced, and turbulent motions with an appropriate turbulence closure scheme. Makin and Mastenbroek (1996) employ the full balance equations of turbulent kinetic energy and its dissipation to calculate drag coefficients over fully developed seas. Balancing local turbulent production and dissipation, *Makin and Kudryavtsev* (1999) estimate an eddy viscosity, which is also used to parameterize the turbulent dissipation rate. Satisfying energy conservation in the WBL, *Hara and Belcher* (2004) relate the turbulent dissipation rate to the reduced turbulent stress, in order to calculate the wind speed profile over mature wave spectra.

1.3 The need to incorporate breaking waves

In most of the previous wind-wave models, only the wind-input to non-breaking waves has been considered (*Komen et al.*, 1996; *Cavaleri*, 2006). A notable exception is the investigation by *Kudryavtsev and Makin* (2001), who estimated that a considerable fraction (up to 50%) of the wind stress can be supported by breaking waves. Their model is based on momentum conservation at the sea surface, where the total stress partitions into the viscous

stress and wave induced stress due to breaking and non-breaking waves. While this study presents significant progress towards understanding the breaking wave effect on air-sea momentum flux, it has important shortcomings. First, the parameterization of the momentum flux from wind to non-breaking waves depends on the total wind stress. To accurately model the stress partitioning, however, it is critical that the parameterization depend on the reduced turbulent stress (*Makin and Kudryavtsev*, 1999; *Kukulka and Hara*, 2005). Second, the mean wind profile in the WBL is prescribed as logarithmic. Such a wind profile generally does not satisfy energy and momentum conservation at each height within the WBL. Third, the energy input to breaking waves is neglected in the wave energy balance. While we adopt their parameterization of the breaking wave form drag, we also will address these short-comings in this study.

To understand the maximum possible influence of breaking waves, we previously devised a model for the extreme case in which the wind input is dominated by breaking waves ((*Kukulka et al.*, 2007), hereafter referred to as KHB). Such a model is applicable to strongly forced wave fields as they have been observed in the laboratory. For older seas (fully developed), however, the model does not yield physical solutions, suggesting that the input to non-breaking waves cannot be neglected for the whole wave spectrum.

To model the form drag of breaking and non-breaking waves, we will combine the model from KHB with the approach from Hara and Belcher (2002, 2004). In the next section, we derive coupled nonlinear advance-delay differential equations governing the wind speed, turbulent wind stress, the wave height spectrum, and the breaking wave distribution. The system of equations is based on the conservation of momentum and energy in the WBL and wave energy conservation. In section 3 the model is applied to idealized mature wind-driven seas, followed by concluding remarks in section 4.

2 Theory

The wave field is described statistically by the two-dimensional wavenumber spectrum $\Psi(k,\theta)$, or alternatively the saturation spectrum, $B(k,\theta) = k^4\Psi(k,\theta)$, and the two-dimensional distribution of breaking waves, $\Lambda(k,\theta)$. The average breaking crest length of waves, at wavenumber k and propagating in the direction θ relative to the wind, is given by $\Lambda(k,\theta)kd\theta dk$ (*Phillips*, 1985). The unitless one-dimensional distribution of breaking waves is defined as

$$\Lambda(k) = \int_{-\pi/2}^{\pi/2} \Lambda(k,\theta)kd\theta. \tag{1}$$

and the unitless one-dimensional saturation spectrum is defined as

$$B(k) = \int_{-\pi/2}^{\pi/2} B(k,\theta)d\theta \tag{2}$$

with the directional spreading (or directionality) of $B(k,\theta)$ defined as

$$h_B(k,\theta) = \frac{B(k,\theta)}{B(k)}, \tag{3}$$

and the directional spreading of $\Lambda(k,\theta)$ defined as

$$h_\Lambda(k,\theta) = \frac{k\Lambda(k,\theta)}{\Lambda(k)}. \tag{4}$$

Here, $\Lambda(k,\theta)$ and $B(k,\theta)$ are assumed to be zero for $|\theta| > \pi/2$ for simplicity.

The geometry of breaking waves, characterized by a steep (nearly discontinuous) slope, differs from the smooth sea surface geometry resulting from non-breaking waves. In order to define a vertical coordinate z above such a complex surface, consider first the instantaneous air-water interface due to the superposition of sinusoidal non-breaking waves with random phase. For such an interface, one may introduce a local, time-varying vertical coordinate z, so that $z = 0$ at the sea surface (z increases with height) (*Makin et al.*, 1995; *Makin and Kudryavtsev*, 1999). Now we superimpose intermittent breaking wave crests as disturbances with finite height above the smooth non-breaking wave surface, such that for a breaking wave at k its crest appears at a height $z = a(k)$, where a is the wave amplitude.

We assume that breaking waves are self similar and that the wind is stationary and horizontally homogeneous with mean wind speed u in the x-direction. The wind velocity vector $(\mathcal{U}, \mathcal{V}, \mathcal{W})$ is decomposed into

$$(\mathcal{U}, \mathcal{V}, \mathcal{W}) = (u + \tilde{u} + u', \tilde{v} + v', \tilde{w} + w'), \tag{5}$$

where the tilde indicates wave-induced motions and the prime denotes turbulent motions.

Furthermore, KHB introduced the "spatial sheltering effect", so that shorter waves in airflow separation areas of longer breaking waves cannot be forced by the wind. *Kukulka* (2006) found overall that the spatial sheltering affects mainly young developing seas. Therefore, for simplicity we neglect the spatial sheltering effect in Part 1, and will examine the effect on young seas in Part 2.

2.1 Air-side momentum conservation

Within the constant stress layer, the total wind stress τ_0 partitions into turbulent Reynolds stress, $\tau_t = -\rho_a \langle u'w' \rangle$, and wave-induced parts (here $\langle \cdot \rangle$ denotes phase averaging and ρ_a is the density of air). The wave-induced stress is decomposed further into one part due to the form drag of non-breaking waves, τ_w, and another part due to the form drag of breaking waves, τ_b. Here, τ_w is referred to as "wave stress" and τ_b as "breaking stress". The breaking stress transfers momentum directly into the wave, so that it effectively reduces the momentum transport through the air inside the WBL. The total momentum budget can be written as

$$\tau_0 = \tau_t(z) + \tau_w(z) + \tau_b(z) = \text{constant}. \tag{6}$$

The wave-induced momentum flux at height z into non-breaking waves is given by (*Makin et al.*, 1995; *Makin and Kudryavtsev*, 1999)

$$\tau_w(z) = \int_0^\infty \int_{-\pi/2}^{\pi/2} \rho_w \omega \beta_g(k, \theta) \Psi(k, \theta) F(z, k) \cos\theta \; k \; d\theta dk, \tag{7}$$

where ρ_w denotes the density of water, β_g is the growth rate of wind-driven gravity waves and $F(z, k)$ is a decay function to account for the decrease in wave induced stress with

height (*Makin et al.*, 1995). The forcing of non-breaking waves depends on the turbulent stress in a thin layer above the water surface, the so called "inner layer" (*Belcher and Hunt*, 1993). The inner layer height is given by δ/k, where δ is the constant inner layer height coefficient. The wave-induced stress also decays over a comparable height. We therefore approximate $F(z,k)$ as a step function, which equals one inside the inner layer and zero outside (*Makin et al.*, 1995; *Makin and Kudryavtsev*, 1999). Furthermore, β_g is set to a form based on empirical estimates (*Plant*, 1982), except that the forcing stress is determined by the turbulent stress evaluated at the inner layer height, rather than the total wind stress (*Makin and Mastenbroek*, 1996; *Belcher*, 1999; *Makin and Kudryavtsev*, 1999), i.e.,

$$\beta_g(k,\theta) = c_\beta \omega \frac{\tau_t(z=\delta/k)}{\rho_w c^2} h_\beta(\theta)\ s[u_*^l(z=\delta/k) - \phi c] \tag{8}$$

where c is the phase speed, $h_\beta = \cos^2\theta$ denotes the directionality of β_g. The step function $s(q)$,

$$\begin{aligned} s(q) &= 1 \qquad \text{for} \qquad q \geq 0 \\ s(q) &= 0 \qquad \text{for} \qquad q < 0 \end{aligned} \tag{9}$$

assures that waves moving faster than a multiple $\phi^{-1} = 1/0.07$ of the local friction velocity $u_*^l(z=\delta/k) = \sqrt{\tau_t(z=\delta/k)/\rho_a}$ are not forced by the wind (*Plant*, 1982). Note that for simplicity, we do not consider the damping of waves with $u_*^l(z=\delta/k) < \phi c$ (see,e.g., *Jenkins* (1992) how wave damping could be incorporated). To keep the notation simple, we define

$$s_\beta = s[u_*^l(z=\delta/k) - \phi c], \tag{10}$$

so that the wave-induced stress becomes

$$\tau_w(z) = \int_0^{\delta/z} \int_{-\pi/2}^{\pi/2} s_\beta c_\beta h_\beta(\theta) \tau_t(z'=\delta/k)\ B(k,\theta)\ k^{-1}\ \cos\theta\ d\theta dk. \tag{11}$$

The form drag of breaking waves is parameterized following Kudryavtsev and Makin (2001) and KHB. For a monochromatic wave with amplitude a and breaking crest length l, the wind force τ_b (per unit ocean surface area) that acts on the breaking wave is

$$\tau_b(k) = -\Delta p(k) 2a(k) l(k), \tag{12}$$

where Δp denotes the pressure drop due to airflow separation ahead of the wave crest. Scaling arguments as well as previous experiments suggest that the pressure drop can be parameterized by

$$\Delta p(k) = -\rho_a c_\gamma [u(k)\cos\theta - c]^2 \; s[u(k)\cos\theta - c] \tag{13}$$

where $u(k) = u(z = \epsilon/k)$ denotes the wind speed evaluated at the height of the breaking wave, $a = \epsilon/k$, ϵ is the slope of the breaking wave, and c_γ is the breaking wave drag coefficient. In this paper we assume for simplicity the linear phase speed of surface gravity wave, although in principle a phase speed factor can be introduced to model the phase speed of nonlinear waves (see also KHB). Similar to the forcing of non-breaking waves, the step function assures that only waves moving with a phase speed slower than $u\cos\theta$ are forced by the wind and for convenience we will introduce a notation

$$s_p = s[u(k)\cos\theta - c]. \tag{14}$$

Assuming that the momentum flux to the breaking wave is concentrated at the wave crest, the breaking wave form drag at height z for a spectrum of waves is expressed as

$$\tau_b(z) = \int_0^{\epsilon/z} \int_{-\pi/2}^{\pi/2} \rho_a s_p \; \beta_\Lambda \; \Lambda(k,\theta) \; [u(k)\cos\theta - c]^2 \; \cos\theta \; d\theta dk, \tag{15}$$

where Λ is the distribution function of breaking waves and $\beta_\Lambda = 2c_\gamma\epsilon$ is a constant coefficient.

2.2 Air-side energy conservation

The total energy equation can be obtained by considering the mean energy budgets of mean, wave-induced, and turbulent motions (*Makin and Mastenbroek*, 1996; *Hara and Belcher*, 2004). We will follow closely the approach by Hara and Belcher (2004) and KHB and emphasize here only how the total energy equation deviates from the traditional model of turbulent shear flow close to a solid wall. Let us start with the total mean energy equation for a turbulent shear flow that is not influenced by waves (*Cohen and Kundu*, 2002),

$$\frac{d(u\tau_t)}{dz} - \frac{d\Pi}{dz} - \varepsilon(z) = 0. \tag{16}$$

The product $u\tau_t$ in the first term describes the energy flux due to the turbulent stress acting on the mean flow, $\Pi = (\overline{p'w'} + \rho_a \frac{1}{2}\overline{w'(u'^2 + w'^2 + v'^2)})$ is the mean vertical energy flux associated with turbulent fluctuations, and the last term, ε, denotes the dissipation rate of turbulent kinetic energy. Similar to traditional turbulence models close to a solid wall, we neglect the divergence of the flux Π in the further analysis. The simulation of airflow over non-breaking waves also suggests that the divergence of Π is not the dominant term in the balance equation of turbulent kinetic energy (*Makin and Mastenbroek*, 1996). Then, the total mean energy equation for traditional wall layer turbulence can be written as

$$\frac{d(u\tau_t)}{dz} - \varepsilon(z) = 0. \tag{17}$$

Based on the observation that eddies lose their kinetic energy roughly during a turning period, the dissipation rate can be estimated by

$$\varepsilon = \frac{\tau_t^{3/2}}{\rho_a^{3/2}\kappa z}, \tag{18}$$

where $\kappa = 0.4$ is the von Kármán constant, $\tau_t = \rho_a[u_*^l]^2 \sim \frac{1}{2}\rho_a(|u'|^2 + |v'|^2 + |w'|^2)$ is a scale for the kinetic energy of the eddy, and $\tau_t^{1/2}(\rho_a^{1/2}\kappa z)^{-1} = u_*^l(\kappa z)^{-1}$ is a scale for the turning frequency (*Cohen and Kundu*, 2002). We will follow Hara and Belcher (2004), who use this parameterization to model the losses of turbulent kinetic energy in the wave boundary layer. Without wave-induced stresses $\tau_t = \tau_0 =$ constant, so that integration of (17) yields the logarithmic wind speed profile.

The effects of waves on the balance (17) are as follows. First, wave-induced energy fluxes, resulting in the transfer of energy from the air to waves, need to be considered. Second, as discussed in the previous subsection, the turbulent stress decreases towards the surface due to wave-induced stresses; therefore, the dissipation rate also decreases towards the surface. Third, the wave stress also acts on the mean flow, so that the energy flux $u\tau_t$ in (17) needs to be replaced by $u(\tau_t + \tau_w)$. The mean air-side energy equation including the wave effect, can be written as

$$\frac{d[u(\tau_t + \tau_w)]}{dz} - \varepsilon(z) - \frac{d\Pi_w}{dz} - e_b(z) = 0, \tag{19}$$

where Π_w denotes the energy flux induced by non-breaking waves and e_b is the rate of air energy transferred to breaking waves. The energy flux due to wave-induced motions, Π_w, is parameterized after Hara and Belcher (2004)

$$\Pi_w(z) = -\int_0^{\delta/z} \int_{-\pi/2}^{\pi/2} I_w(k,\theta) k \; d\theta dk. \tag{20}$$

where

$$I_w(k,\theta) = c_\beta s_\beta h_\beta(\theta) \; k^{-2} \; c \; \tau_t(z = \delta/k) \; B(k,\theta) \tag{21}$$

is the spectral energy flux to non breaking waves.

Following KHB, the spectral energy flux to breaking waves is

$$I_b(k,\theta) = \rho_a s_p \beta_\Lambda \;\; \Lambda(k,\theta) \; k^{-1} \; c[u(k)\cos\theta - c]^2, \tag{22}$$

and the angle integrated spectral energy flux is

$$I_b(k) = \; c \; \int_{-\pi/2}^{\pi/2} \rho_a s_p \beta_\Lambda \; \Lambda(k,\theta) \; [u(k)\cos\theta - c]^2 \; d\theta. \tag{23}$$

Since the energy is mostly transferred at the breaking wave height $a = \epsilon/k$, one finds

$$e_b(z)dz = -I_b(k)dk. \tag{24}$$

2.3 Wave energy conservation

In the equilibrium range for waves with wavenumbers between k_0 and k_1 (here we define k_0 and k_1 as the lower and upper bound wavenumber, respectively), the wave field is stationary and homogeneous, so that the energy input rate due to wind forcing is balanced by the wave dissipation rate, D, and nonlinear interactions, NL,

$$I_w(k,\theta) + I_b(k,\theta) + NL(k,\theta) - D(k,\theta) = 0, \tag{25}$$

where I_w and I_b were specified in the previous subsection. Following Phillips (1985), we set

$$NL \;\; = \;\; \rho_w \; (\gamma_\Lambda - \gamma_3) \; c^3 \; k^{-2} [B(k,\theta)]^3, \tag{26}$$

$$D \;\; = \;\; g^{-1} \rho_w b \; c^5 \; \Lambda(k,\theta). \tag{27}$$

The parameterization of the nonlinear interaction term is based on resonant interaction of four gravity waves, where the constant coefficients γ_3 and γ_Λ are similar to Phillips' β and γ, respectively. The parameterization of the dissipation term is based on the loss of energy of a breaking wave front to turbulence and b is a constant coefficient.

2.4 $\Lambda(B)$

In order to solve the above equations for B, Λ, τ_t, and u, one must prescribe a functional relationship between Λ and B. We set

$$\Lambda(k,\theta) = \gamma_\Lambda b^{-1} k^{-1} [B(k,\theta)]^3 \left(1 + \left[\frac{B(k,\theta)}{B_{sat}}\right]^n\right), \tag{28}$$

where $n \gg 1$. In the limit $n \to \infty$, $\Lambda \propto B^3$ for all $B < B_{sat}$ and $\Lambda \to \infty$ for all $B > B_{sat}$. The first term of the sum is based on the arguments that there is a wavenumber range in which nonlinear interactions and dissipation are proportional to each other (*Phillips*, 1985). The second term of the sum is based on the observation that Λ increases rapidly for $B > B_{sat}$ (*Banner et al.*, 2002), where B_{sat} is the "threshold saturation level" (*Alves and Banner*, 2003). Notice that the first term on the right hand side is dominant for $B < B_{sat}$, while the second term dominates for $B \geq B_{sat}$. Hence, from (26) and (27) one obtains
for $B(k,\theta) < B_{sat}$

$$NL - D = -\gamma_3 \rho_w k^{-2} c^3 [B(k,\theta)]^3 \tag{29}$$

and for $B(k,\theta) \to B_{sat}$

$$NL - D = \rho_w \ (\gamma_\Lambda - \gamma_3) \ c^3 \ k^{-2} B_{sat}^3 - g^{-1} \rho_w b \ c^5 \ \Lambda(k,\theta). \tag{30}$$

From the wave energy equation (25) with (22) and (21), one may express B and Λ in terms of wind properties for $B(k,\theta) < B_{sat}$ and $s_\beta = 1$

$$B(k,\theta) = \left(c_\beta b \ h_\beta(\theta) \ \frac{\tau_t(z = \delta/k)}{\rho_w b \gamma_3 c^2 - s_p \beta_\Lambda \gamma_\Lambda \rho_a (u\cos\theta - c)^2}\right)^{1/2} \tag{31}$$

$$\Lambda(k,\theta) = \gamma_\Lambda b^{-1} k^{-1} [B(k,\theta)]^3 \tag{32}$$

and for $B(k,\theta) \rightarrow B_{sat}$

$$B(k,\theta) = B_{sat} \tag{33}$$

$$\Lambda(k,\theta) = \frac{s_\beta c_\beta \ \tau_t(z=\delta/k) \ h_\beta(\theta) + \rho_w \ (\gamma_\Lambda - \gamma_3) \ c^2 \ B_{sat}^2}{\rho_w b \ c^2 \ - s_p \beta_\Lambda \ [u(k)\cos\theta - c]^2 \ \rho_a} B_{sat} k^{-1}. \tag{34}$$

Note that the equilibrium range spectrum for short waves (33) is consistent with the equilibrium range model used by *Jenkins* (1993) to calculate momentum air-sea fluxes.

2.5 Governing advance-delay equations

2.5.1 Relation between height and wavenumber

Unlike the models of Hara and Belcher (2002, 2004) or KHB, which consider the wind input to either breaking or non-breaking waves, at height z momentum and energy can be transferred to waves at two different wave scales. To determine changes in the air momentum and energy balances, (6) and (19), respectively, from height z to height $z + dz$, momentum and energy is transferred to non-breaking waves at a wavenumber $k = \delta/z$ and to breaking waves at a wavenumber $k = \epsilon/z$. Furthermore, consider the wind input terms in the wave energy equation (25) at a single wavenumber k. The input term to non-breaking waves (21) requires the turbulent stress evaluated at the inner layer height $z = \delta/k$. In contrast, the input term to breaking waves (22) depends on the wind speed evaluated at the wave height of the breaker $z = \epsilon/k$. In the following discussion, we will derive the governing advance-delay equations, reflecting that derivatives in z (or in k) of the turbulent stress and wind speed at a given height (or wave scale) depends on terms evaluated at lower and higher heights as well (or smaller and grater wave scales).

The breaking height $z = a(k) = \epsilon/k$ can be uniquely related to k, so that

$$z(k) = \frac{\epsilon}{k}. \tag{35}$$

Furthermore, we define the turbulent stress evaluated at the breaking height

$$\tau_t(k) = \tau_t(z = \epsilon/k) \tag{36}$$

and the ratio of the inner layer height and the breaking height

$$\delta_\epsilon = \frac{\delta}{\epsilon} < 1. \tag{37}$$

Substitution of (11) and (15) into (6) yields, after differentiation with respect to k,

$$\begin{aligned}\frac{d(\tau_t)}{dk} + \int_{-\pi/2}^{\pi/2} \rho_a s_p \beta_\Lambda \ \Lambda(k,\theta) \ [u(k)\cos\theta - c]^2 \cos\theta \ d\theta \\ + \int_{-\pi/2}^{\pi/2} s_\beta c_\beta h_\beta(\theta) \tau_t(k) \ B(\delta_\epsilon k, \theta) \ k^{-1} \ \cos\theta d\theta = 0.\end{aligned} \tag{38}$$

Substitution of (20) and (23) into (19) yields

$$\begin{aligned}\frac{d[u(\tau_t + \tau_w)]}{dk} + \int_{-\pi/2}^{\pi/2} \rho_a s_p \beta_\Lambda \ \Lambda(k,\theta) \ c[u(k)\cos\theta - c]^2 \ d\theta \\ + \int_{-\pi/2}^{\pi/2} c(\delta_\epsilon k) s_\beta c_\beta h_\beta(\theta) \tau_t(k) \ B(\delta_\epsilon k, \theta) \ k^{-1} \ d\theta + \frac{\tau_t^{3/2}}{\kappa k \rho_a^{1/2}} = 0.\end{aligned} \tag{39}$$

Note that $\delta_\epsilon k$ refers to a longer wave with an inner layer height $z = \epsilon/k$. The wave energy equation (25) becomes

$$\begin{aligned}\rho_a s_p \beta_\Lambda \ \ \Lambda(k,\theta) \ c[u(k)\cos\theta - c]^2 \ \ &+ \ \ s_\beta c_\beta h_\beta(\theta) \ c \ \tau_t(k/\delta_\epsilon) \ B(k,\theta) \ k^{-1} + \\ \rho_w \ (\gamma_\Lambda - \gamma_3) \ c^3 \ k^{-1} [B(k,\theta)]^3 \ \ &= \ \ \rho_w b \ c^3 \ \Lambda(k,\theta).\end{aligned} \tag{40}$$

Note that the turbulent stress evaluated at the inner layer height δ/k is $\tau_t(k/\delta_\epsilon)$.

To solve these last three equations for wavenumbers between k_0 and k_1 (corresponding to breaking wave amplitudes of ϵ/k_1 to ϵ/k_0), one needs to specify B between $\delta_\epsilon k_0$ and k_0 in equations (38) and (39). Furthermore, to solve the wave energy equation (40) for waves between k_0 and k_1, one needs to specify $\tau_t(k)$ between k_1 and k_1/δ_ϵ.

2.5.2 Non-dimensional variables

We introduce the following non-dimensional variables,

$$dK = \frac{dk}{k} \tag{41}$$

$$S = \frac{\tau_t}{\rho_a c^2} \tag{42}$$

$$S_w = \frac{\tau_w}{\rho_a c^2} \tag{43}$$

$$U = \frac{u}{c} \tag{44}$$

$$b' = \frac{\rho_w}{\rho_a} b. \tag{45}$$

Here, K is the non-dimensional wavenumber linear in $\log k$, S is the normalized turbulent stress, S_w is the normalized wave stress, and U is the normalized mean wind speed. Furthermore, the following model parameters are defined:

$$\gamma^2 = \frac{\beta_\Lambda}{b'} \tag{46}$$

$$\mu^2 = \frac{\rho_a c_\beta^3}{\rho_w \gamma_3} \tag{47}$$

$$\mu_\Lambda^2 = \frac{\rho_a c_\beta^3}{\rho_w \gamma_\Lambda} \tag{48}$$

$$n_{NL} = \frac{\gamma_3 - \gamma_\Lambda}{\gamma_3} \qquad \text{(fraction of } NL \text{ input)} \tag{49}$$

$$\mu_\Lambda = \frac{\mu}{\sqrt{1 - n_{NL}}} \tag{50}$$

$$\Delta = -\log(\delta_\epsilon) > 0. \tag{51}$$

The first terms in (38) and (39) become

$$\frac{d(\tau_t)}{dk} = c^2 k^{-1} \rho_a \left(\frac{dS}{dK} - S \right), \tag{52}$$

$$\begin{aligned} \frac{d[u(\tau_t + \tau_w)]}{dk} &= (\tau_t + \tau_w)\frac{du}{dk} + u\frac{d\tau_b}{dk} \\ &= c^3 k^{-1} \rho_a \left[(S + S_w) \left(\frac{dU}{dK} - \frac{1}{2} U \right) - U c^{-2} \rho_a^{-1} \frac{d\tau_b}{dK} \right]. \end{aligned} \tag{53}$$

After multiplying equation (38) by $\rho_a^{-1} k c^{-2}$ and (39) by $\rho_a^{-1} k c^{-3}$, the non-dimensional air momentum and air energy equations are expressed as

$$\frac{dS}{dK} = S - M_b - M_w \tag{54}$$

$$\frac{dU}{dK} = \frac{1}{2} U - (S + S_w)^{-1} \left(E_b + \delta_\epsilon^{-1/2} E_w - U M_b + \kappa^{-1} S^{3/2} \right) \tag{55}$$

which need to be solved for S and U. Note that the equation for U contains S_w which is calculated as

$$\frac{dS_w}{dK} = S_w + M_w. \tag{56}$$

The normalized flux terms in the governing non-dimensional equations are

$$M_b = \int_{-\pi/2}^{\pi/2} s_p[k\beta_\Lambda\ \Lambda(K,\theta)]\ [U\cos\theta - 1]^2 \cos\theta\ d\theta \tag{57}$$

$$M_w = S\int_{-\pi/2}^{\pi/2} s_\beta c_\beta B(K-\Delta,\theta)\ h_\beta(\theta)\ \cos\theta d\theta \tag{58}$$

$$E_b = \int_{-\pi/2}^{\pi/2} s_p[k\beta_\Lambda\Lambda(K,\theta)]\ [U\cos\theta - 1]^2\ d\theta \tag{59}$$

$$E_w = S\int_{-\pi/2}^{\pi/2} s_\beta c_\beta\ B(K-\Delta,\theta)\ h_\beta(\theta)\ d\theta \tag{60}$$

From the wave energy equation (40) and the relation $\Lambda(B)$ from (28), one further obtains expressions for B and Λ in non-dimensional variables.

For $B(K,\theta) < B_{sat}$ and $s_\beta = 1$

$$c_\beta B(K,\theta) = \left(\delta_\epsilon S(K+\Delta)\ \frac{h_\beta(\theta)}{\mu^{-2} - \gamma^2\mu_\Lambda^{-2} s_p(U\cos\theta - 1)^2}\right)^{1/2} \tag{61}$$

$$k\beta_\Lambda\Lambda(K,\theta) = \gamma^2\mu_\Lambda^{-2}[c_\beta B(K,\theta)]^3. \tag{62}$$

For $B(K,\theta) \to B_{sat}$

$$c_\beta B(K,\theta) = c_\beta B_{sat} \tag{63}$$

$$k\beta_\Lambda\Lambda(k,\theta) = \frac{\gamma^2\delta_\epsilon h_\beta(\theta)\ s_\beta S(K+\Delta) + \gamma^2(\mu_\Lambda^{-2} - \mu^{-2})(c_\beta B_{sat})^2}{1 - \gamma^2\ s_p[U\cos\theta - 1]^2} c_\beta B_{sat}. \tag{64}$$

In summary, our coupled wind wave model is described by the three coupled first-order differential equations for the three variables S, U, and S_w.

The model equations (54) to (64) have the following important properties. First, with $\gamma = 0$ and $B_{sat} \to \infty$ the governing equations converge to the system without breaking waves (*Hara and Belcher*, 2002, 2004). With $\gamma = 0$, but limiting B_{sat}, the solutions are modified (part 2). Second, for $c_\beta = 0$, the system (54) to (64) equals the model with input to breaking waves only (KHB). Third, although the system (54) to (64) is fully coupled, the air-side equations (54) to (60) can be solved for any known wave field, Λ and B without (61) to (64). In this case, only the input coefficients β_Λ, ϵ for breaking waves and c_β, δ for

non-breaking waves need to be specified. Furthermore, for given Λ and B, solutions will be self-similar in $c_\beta B$, $\beta_\Lambda \Lambda$.

In solving the full system (54) to (64), the term $S(K + \Delta)$ in (61) and (64) introduces an "advance" term. In addition, evaluation of (58) and (60) using (61) introduces a "delay" term $U(K - \Delta)$. To understand the physical origin of the advance-delay terms see also the discussion of the previous subsection. The solution to such advance-delay equations differs from solutions of ordinary differential equations, since the solution depends not only on the boundary conditions at some k with $k_0 \leq k \leq k_1$, but generally also on some specified S for $k > k_1$ and specified U for $k < k_0$. As there are no standard solvers for advance-delay equations available, we propose a simple method of solution in the Appendix A.

2.6 Estimates of parameters

In this section we will show that model results depend on six key parameters: two height coefficients, two wave input coefficients, and two coefficients that are related to the wave height spectrum. Originally, the model depends on eight physical coefficients c_β, δ, γ_3, γ_Λ, B_{sat}, β_Λ, ϵ, and b. For the normalized system of equations, the number of coefficients is reduced to five model parameters Δ, $c_\beta B_{sat}$, μ, μ_Λ, and γ. We will next consider how this multi-dimensional parameter space can be constrained in a physically meaningful way.

First, the effect of the non-linear wave-wave interactions ($\gamma_3 \neq \gamma_\Lambda$ and $\mu \neq \mu_\Lambda$) will be analyzed in detail only in subsection 3.4, so that $\gamma_3 = \gamma_\Lambda$, and $\mu = \mu_\Lambda$ unless noted otherwise.

Second, although there are two physical coefficients, β_Λ and b, related to the breaking wave dynamics, they affect just one model parameter $\gamma = \sqrt{\beta_\Lambda \rho_a / b \rho_w}$ that depends on the ratio of the two. In fact, γ can be interpreted as a measure of net energy and momentum input to breaking waves. The following discussion is therefore focused on this parameter γ instead of β_Λ and b. The value of b will be only necessary for determining the absolute value of the breaking statistics Λ for comparison with observations. We set $b = 0.01$ for that purpose, which is consistent with the range (from 0.003 to 0.07) estimated by *Melville* (1996).

Third, the physical coefficient γ_3 and the model coefficient μ are both related to the Phillips (1985) wave height spectrum coefficient α_p, which determines the wave spectrum level closer to the spectral peak (see Appendix C).

In summary, our solutions involve six critical parameters with clear physical interpretation: two height coefficients ϵ and δ, determining the input heights to breaking and non-breaking waves; two input coefficients γ and c_β for breaking and non-breaking waves; and two coefficients μ and B_{sat}, controlling the spectral level. These six physical parameters then determine the four model parameters, Δ, $c_\beta B_{sat}$, μ, and γ.

2.6.1 Two height coefficients

The input height coefficient to breaking waves is the breaking wave slope, which ranges from 0.1 to 0.5 (*Melville*, 1996) and is held constant at the intermediate value $\epsilon = 0.3$ in this study. The coefficient δ is less constrained: previous studies have assumed values approximately between $\delta = 0.01$ and 0.1. Here, the value of $\delta = 0.05$ is adopted (*Hara and Belcher*, 2004).

2.6.2 Two input coefficients

Based on observations, the proportionality coefficient of the wave growth rate was estimated to be $c_\beta = 32 \pm 16$ (*Plant*, 1982). Because many theoretical studies indicate that c_β is close to 16 for gravity waves (*Belcher and Hunt*, 1998), c_β is set to $c_\beta = 25$, which is between the average value from observations and theoretical estimates. The value of the input coefficient to breaking waves γ is difficult to constrain since our knowledge of the breaking wave dynamics is limited. In this study we set $\gamma = 0.07$ so that our model results of the Charnock coefficient agree with previous observations (see section 3.3). This value is also consistent with the previously estimated range $\gamma = 0.04 - 0.5$ (KHB). The model dependence on different values of γ is discussed in part 2.

2.6.3 Two wave spectrum coefficients

The coefficient B_{sat} is the threshold of $B(k,\theta)$ where dissipation limits the saturation spectrum. Recent field observations suggest that B_{sat} is in the range $0.001 < B_{sat} < 0.005$ with most values likely between $0.001 < B_{sat} < 0.003$ (Appendix C). Most observations of the Phillips (1985) wave height spectrum coefficient range from $\alpha_p = 0.06$ to $\alpha_p = 0.13$ (*Hwang et al.*, 2000a), but α_p can be as low as $\alpha_p = 0.02$ (*Hara and Belcher*, 2004). Based on the analysis in Appendix C, this results in a range of μ between 0.125 and 0.813. Since the wave field, and therefore α_p and B_{sat}, likely depend on wind speed and sea state, α_p and B_{sat} generally cannot be assumed constant (*Komen et al.*, 1996). We will therefore examine our model results over the ranges of $0.001 < B_{sat} < 0.005$ and $0.125 < \mu < 0.813$ (with the default values of $B_{sat} = 0.002$ and $\mu = 0.6$) in the following discussion.

In summary, we will fix the two model coefficients $\Delta = 1.8$ and $\gamma = 0.07$ and let the other two model coefficients, $c_\beta B_{sat}$ and μ, vary corresponding to the uncertainty of the wave spectrum coefficients α_p and B_{sat}. Note that if B and Λ were known, only the four coefficients β_Λ, c_β, ϵ and δ are required to solve the air-side equations (54) to (60).

3 Mature seas

Applying our model to mature, pure wind-seas allows an important simplification. Mature seas can be classified by a wave age criterion (*Drennan et al.*, 2003),

$$\sigma = \frac{c_p}{u_*} > 20, \tag{65}$$

where σ is the wave age and c_p is the phase speed at the spectral peak. Since the peak wavenumber $k_p < g u_*^{-2} 20^{-2}$ is smaller than $g u_*^{-2} \phi^2$ (ϕ is described in (8)), non-breaking waves close to the spectral peak are not forced by the wind. If we set $k_0 = g u_*^{-2} \phi^2$, the delay terms in (58) and (60) vanish in the range $\delta_\epsilon k_0 < k < k_0$, allowing us to integrate the system of equations from $k = k_0$. Furthermore, as our results below indicate, for the longest waves the dissipation of wave energy and the input to breaking waves for $k < k_0$ is

negligible. Therefore, one may practically set the wind input and dissipation for all waves with $k < k_0$ to zero. If k_0 is far enough from the peak, so that complex dynamics close to the peak do not significantly influence the simple wave energy balance (25), then our model can be applied for the entire wind forced range of mature sea spectra.

The wind speed at the surface is for mathematical convenience set to zero, i.e., $u = 0$ at $k_1 \to \infty$. Physical solutions need to be truncated at a finite k_1, where the effects of viscosity or surface tension are significant. Previous studies have shown that the solution is not very different if k_1 is set above 400m^{-1} for medium to high wind speeds (*Hara and Belcher*, 2004). Details on the method of finding solutions to the advance-delay differential equations are presented in Appendix A. We will first thoroughly discuss the solutions for the wave field, which is critical to the accurate determination of wave-induced fluxes.

3.1 Surface wave height spectrum

Before considering the full two dimensional wave height spectrum, we focus the discussion on the angle-integrated, one-dimensional, wave height spectrum.

3.1.1 One-dimensional

A sensitivity analysis indicates that the shape of the spectrum depends mainly on the parameter μ (or α_p for fixed c_β) and B_{sat}. The parameter μ determines the spectral level at low k, while B_{sat} determines the spectral level at high k. The spectral level increases with increasing B_{sat} and μ. Figure 1 shows the possible range of one-dimensional wave curvature saturation spectra, corresponding to the lowest and highest values of B_{sat} and μ. Solutions of the marginal saturation spectrum are also compared to previous observations (*Melville and Matusov*, 2002; *Banner et al.*, 1989) in Figure 2.

Our results show a distinct high and low wavenumber part, which is due to the two regimes of the Λ function (28). At low wavenumbers, where the wind-input is proportional to nonlinear interactions, the saturation spectrum roughly increases as $k^{1/2}$, similar to the Phillips (1985) spectrum. As B increases to B_{sat} at higher wavenumbers, dissipation by wave

breaking limits B to B_{sat}, so that B approaches a constant value at B_{sat}. This is equivalent to the hard limit of B first proposed by Phillips (1958). Therefore, this asymptote differs physically from the asymptote found by Hara and Belcher (2002), which is due to spectral sheltering. Theoretically, if B_{sat} exceeds the asymptotic limit of Hara and Belcher (2002), B cannot reach B_{sat} and the model is independent of B_{sat}. However, our upper bound of $B_{sat} = 0.005$ is still lower than the limit of Hara and Belcher (2002). The transition wavenumber between the two regimes depends on both μ and B_{sat}. Interestingly, the wave spectrum is quite robust and insensitive to other model parameters.

3.1.2 Two-dimensional

Even though breaking waves generally play an important role in the balance (25), the wave height spectrum is hardly affected by breaking waves for mature seas. This is because at low wavenumbers, breaking waves do not dominate the wind input, as simple scaling arguments suggest (see Appendix B). For high k, on the other hand, B has already reached its constant limit, i.e. it is not affected by the details of the dynamics described by the system (38) to (40). In Appendix C, we show that the saturation spectrum increases with k and is approximated by

$$B(k,\theta) = \frac{1}{4}\alpha_p \frac{u_*}{c}\cos\theta \tag{66}$$

until it reaches B_{sat} and then remains constant afterwards:

$$B(k,\theta) = B_{sat}. \tag{67}$$

Figure 1 indicates that these approximations are indeed very close to the solution of the full model.

The approximate solution for $B(k,\theta)$ yields a cosine distribution of the directional spreading for lower k. For high k, the directional spreading is nearly omnidirectional (Figure 3). Qualitatively, this behavior of the spreading function is consistent with previous observations of wind-driven gravity waves close to the spectral peak (*Hwang et al.*, 2000b) and short wave

spectra (*Banner et al.*, 1989).

3.2 Breaking wave distribution

The other critical statistics concerning the wave field in the coupled wind and wave problem is the distribution of breaking waves. Again, we will first focus on the angle integrated distribution and then discuss the two-dimensional breaking wave distribution.

3.2.1 One-dimensional

Since the normalized governing equations yield the solution of $b'\Lambda(k)$ instead of $\Lambda(k)$, we first present $b'\Lambda(k)$ for different B_{sat} and μ in Figure 4. For any fixed wavenumber, $b'\Lambda$ does not change by more than an order of magnitude due to the uncertainties in the parameters μ and B_{sat} in the examples shown in Figure 4. Close to the spectral peak, the input to breaking waves is negligible (Appendix B). If B can be approximated by (66), Λ is proportional to $k^{3/2}$, which is indeed observed for most cases. Although there is no simple systematic behavior of Λ at higher wavenumbers, the solutions roughly transition from $k^{3/2}$ to k^1 as k increases.

Next, we compare our modeled breaking distribution with the observations from *Melville and Matusov* (2002) (Figure 5), which were obtained for developed seas with wave ages exceeding 20. Since the motion of whitecaps was observed, the measurements of Λ are presented as a function of phase speed, so that we apply the conversion $\Lambda(k)dk = -\Lambda(c)dc$ using the linear dispersion relation. For high phase speeds (low wavenumbers) model results are lower but within an order of magnitude of the observations. Note that our results can be easily increased by adjusting the parameter b. Also, the agreement for greater c is closer, if one assumes an enhanced phase speed of non-linear waves. For these longer waves, we also approximately recover the $\Lambda \sim c^{-6}$ trend found in the observations if $B < B_{sat}$. Note that longer, faster waves that are not directly forced by the wind, should not be compared to theoretical estimates based on a balance between wind input and dissipation. For small phase speeds (high wavenumbers) the power increases for both observations and model results.

However, the observations converge asymptotically to a c^{-1} trend (*Melville and Matusov*, 2002), while the modeled Λ roughly transitions to c^{-5}.

What are possible reasons for this discrepancy at high wavenumbers? First, one must keep in mind the different definitions of Λ. Our Λ is defined based on theoretical ideas, namely that breaking waves can be directly related to dissipation and wind input. This is fundamentally different from the definition based on experiments (*Melville and Matusov*, 2002), which is founded on the idea that the advance of a whitecap represents a breaking wave crest. Especially for short waves, these definitions might be inconsistent, considering for example micro-scale breakers, which do not entrain air. Only more observations will tell if the discrepancy is due to different definitions of Λ, or if there are shortcomings in our theory or the previous experiment (*Melville and Matusov*, 2002).

It is also interesting to compare our model results to previous theoretical studies. For the default parameters, the high c asymptote c^{-6} (or $\Lambda(k) \propto k^{3/2}$) is consistent with previous models (*Phillips*, 1985; *Hara and Belcher*, 2002), where the energy loss due to breaking is balanced by nonlinear interactions of four gravity waves. The calculated low c asymptote for default parameters is close to c^{-5}, which is different from the asymptote c^{-3} found by *Hara and Belcher* (2002). Generally, the asymptotic behavior depends on the model parameters, as we show in part 2.

3.2.2 Directionality

Figure 6 indicates that the functional form of the directionality depends on the model parameters. For larger values of B_{sat} the directionality of the breaking wave distribution changes relatively little with wavenumber. Close to the peak, the directionality approaches a $\cos^3\theta$ distribution for $B(k,\theta) < B_{sat}$ and a $\cos^2\theta$ distribution for $B(k,\theta) \to B_{sat}$. Therefore, if B approaches B_{sat} with increasing k, the directional spreading broadens slightly. For lower B_{sat}, the directional spreading changes little up to $k/k_0 \sim 10^3$ and then narrows as k further increases until Λ becomes unidirectional for the asymptotic limit $k \to \infty$. Note that waves with $k/k_0 > 10^3$ are likely outside the surface gravity wave range for fully developed seas.

This asymptotic limit plays an important physical role, however, for younger growing seas (see part 2).

Our result that the dominant propagation direction of breaking waves is close to the wind direction ($\theta = 0$) is qualitatively consistent with the observations from *Melville and Matusov* (2002). However, more observations are needed to determine if our theoretical framework is sufficient to model the distribution of breaking waves realistically.

3.3 Air-sea momentum flux

The wave field described by the breaking wave distribution and wave height spectrum is critical in determining the wave-induced momentum fluxes. The momentum flux is often parameterized in terms of the drag coefficient c_D that relates the total stress to the wind speed at 10 m height,

$$u_*^2 = c_D U_{10}^2. \tag{68}$$

For a neutrally stable atmosphere, the wind speed profile outside the wave boundary layer is logarithmic

$$U_{10} = \frac{u_*}{\kappa} \ln \frac{h_{ref}}{z_0}, \tag{69}$$

where z_0 is the roughness length and the reference height is $h_{ref} = 10\text{m}$. The Charnock coefficient is a normalized roughness length

$$r = \frac{z_0 g}{u_*^2}. \tag{70}$$

Connecting the wind profile of the wave boundary layer to the logarithmic profile at $z = \epsilon/k_0$ yields

$$r = \epsilon \phi^{-2} \exp\left(-\kappa \phi^{-1} U_0\right), \tag{71}$$

where $U_0 = U(k_0)$ and ϕ has been defined in (8). To calculate the Charnock coefficient, we will assume that the wind stress is mainly supported by the form drag of gravity waves. This assumption is approximately valid for moderate to high wind conditions ($U_{10} > 10\text{ms}^{-1}$), since the relative contribution of the viscous stress decreases with increasing wind speed

(*Komen et al.*, 1996). Furthermore, for mathematical convenience, we consider asymptotic solutions with $k_1 \to \infty$. Previous model results justify this assumption, because model results closely approached this asymptotic limit for $k_1 = 400\text{m}^{-1}$ or larger (*Hara and Belcher*, 2004).

The sensitivity of momentum flux calculations on the input height coefficients δ and ϵ as well as the input coefficients c_β and γ is thoroughly discussed in *Kukulka* (2006). Here, we will adjust γ to be consistent with previous observations of the Charnock coefficient. Generally, observed Charnock coefficients for fully developed seas (with $\sigma = 20 - 30$) have large uncertainties; observations to date span the range $r = 0.008 - 0.5$ (*Jones and Toba*, 2001). Aside from the fact that r might not be uniquely related to σ even for pure wind-seas, part of this wide range is due to significant measurement errors as well as measurements taken for confused seas or unsteady wind conditions. Keeping in mind the large uncertainty, we will next discuss "mean" values, based on best fits to the scattered observations. A best fit to compiled data sets taken prior to 2000 yields a Charnock coefficient between $r = 0.014$ and $r = 0.037$ for fully developed seas (*Jones and Toba*, 2001). Focusing on single-peaked wave spectra from a particular field program, results in a Charnock coefficient between 0.016 and 0.024 (*Smith et al.*, 1992). This range agrees with $r = 0.018$, which accurately models the momentum transfer from wind to ocean for a different field experiment (*Johnson et al.*, 1998). More recently, for carefully selected data sets of pure wind seas, Charnock coefficients have been determined to be $r \approx 0.01$ for $\sigma = 20$ (with most observations in the range of $r = 0.004 - 0.05$) (*Drennan et al.*, 2003). The most recent empirical formula based on the compilation of major data sets from field campaigns yields $r = 0.016, 0.021$ for $U_{10} = 10, 20\text{ms}^{-1}$, respectively (personal communication with Prof. James Edson).

Based on these previous investigations, we may assume that the Charnock coefficient for fully developed seas takes a value close to $r = 0.015$ for mean observed conditions. Imposing a normalized roughness length of $r = 0.015$ for mature ocean conditions, results in a breaking wave input coefficient of $\gamma = 0.07$ with the default values of the wave spectrum coefficients, $\mu = 0.6$ and $B_{sat} = 0.002$. Therefore, we have set by default $\gamma = 0.07$ throughout this study. This value of γ is within the estimated range of KHB, but lower than their default value.

In the following subsection we will show that the momentum flux to breaking waves depends critically on the wave height spectra.

3.3.1 Effect of wave height spectrum

As discussed above, measured wave height spectra show some variability in the parameters μ (or α_p) and B_{sat}, which determine the spectral levels at low and high k, respectively. Systematic changes of μ and B_{sat} with environmental conditions result in variations of r. We therefore investigate the sensitivity of momentum flux calculations towards the combination of minimum and maximum values for the parameters μ and B_{sat} (first nine rows and first five columns in Table 1). Generally, an elevated saturation spectrum (elevated μ and B_{sat}) increases the momentum fluxes into non-breaking waves and enhances the total momentum flux, while the relative input to breaking waves decreases. For $B_{sat} \leq 0.002$, the limiting value B_{sat} is quickly reached so that the value of μ has only a small effect on the overall momentum flux. The specific values of B_{sat} and μ determine, whether the wave form drag is dominated by breaking or non-breaking waves. For example, with $\mu = 0.6$ (default) and $B_{sat} = 0.005$ the momentum flux to non-breaking waves dominates. With the same μ, but $B_{sat} = 0.001$, on the other hand, the input is dominated by breaking waves.

3.3.2 Comparison to models without breaking waves

Starting from the theory without input to breaking waves and $B_{sat} \rightarrow \infty$ (*Hara and Belcher*, 2002, 2004), modeled Charnock coefficients are 0.011-0.093 (last three rows of the last column in Table 1), somewhat larger than mean observations. If we introduce the limiting $B_{sat} = 0.002$, but still neglect the input to breaking waves, modeled Charnock coefficients are now too low (0.002-0.004). Only if the input to breaking waves is included, does the modeled Charnock coefficient increase to 0.011 - 0.015 and agree with observations. Interestingly, an elevated B_{sat} could compensate for neglecting the breaking wave effect to yield a Charnock coefficient that is consistent with observations, although the wind input to the wave field would be physically very different (for example, compare r with and without breaking waves

for $B_{sat} = 0.002$ and $B_{sat} \to \infty$ with $\mu = 0.125$, fourth and tenth row in Table 1). Without the effect of breaking waves, the total momentum flux is more sensitive to the spectral level at high k. Overall, our results indicate that the spectral shape as well as modeling the input to breaking waves is critical to determine the total air-sea momentum flux.

3.3.3 Wind speed and stress profiles

Figures 7 to 9 shows the modeled wind speed and stress partitioning as a function of z normalized by the wave boundary layer height $z_T = \epsilon/k_0$. These results clearly indicate that the input to both breaking and non-breaking waves is significant. Note that near the wave boundary layer height ($z/z_T \approx 1$) the solution for the turbulent stress follows closely the previous theoretical estimate (*Hara and Belcher*, 2002), indicating the dominance of non-breaking waves for longer waves. At very low levels, on the other hand, the wind speed follows approximately the analytic solution from KHB, suggesting that breaking waves dominate the wave energy input for very short waves. Figure 7 indicates that a significant fraction is fluxed to short breaking waves very close to the surface.

Although our solution has been obtained without a fixed wavenumber upper limit ($k_1 \to \infty$), the theory should not be applied in the capillary wave range or in the viscous sublayer. The height of the viscous sublayer can be estimated by $z_\nu \approx 5\nu_a u_{*\nu}^{-1}$, where ν_a denotes the kinematic viscosity of air and $u_{*\nu}$ is the viscous friction velocity (*Cohen and Kundu*, 2002). For $u_* = 1\text{ms}^{-1}$ ($U_{10} \approx 20\text{ms}^{-1}$) and a viscous stress close to 25% of the total stress (see Figure 7), we find $z_\nu/z_T = 5\epsilon^{-1}\nu_a g\phi^2 u_*^{-2} u_{*\nu}^{-1} \approx 2 \times 10^{-5}$, which is close to the lowest heights shown in Figure 7. Therefore, only the input heights of the smallest forced waves shown in Figure 7 are close to the viscous sublayer height. Note that z_ν/z_T further decreases with increasing wind speed.

Next we consider the amplitude z_c of the smallest breaking gravity wave. Assume the shortest breaking wave is at $k_1 = 360\text{m}^{-1}$, so that the normalized input height to breaking waves is given by $z_c/z_T = k_0/k_1 \approx 10^{-4}$ for $u_* = 1\text{ms}^{-1}$. Therefore, the lowest part of Figure 7 may be modified due to the capillary effect. Note that at this height the wave-form drag

contributes about 50% to the total stress. Furthermore, z_c/z_T decreases with increasing u_*, so that the total wave-form drag must increase with u_* (Figure 7). In particular, Figure 7 indicates that the relative contribution of breaking waves to the total wave form drag increases with wind speed.

KHB and *Kukulka* (2006) have shown that the spatial sheltering effect can modify the dynamics close to the surface, and therefore the details of the wind speed and stress partitioning. However, the sheltering hardly affects the drag coefficient of mature seas.

3.4 Nonlinear wave-wave interactions

Nonlinear wave-wave interactions are parameterized by (26) with $\gamma_\Lambda \neq \gamma_3$. Nonlinear interaction alters Λ for longer waves because nonlinear interactions and dissipation are proportional to one another, and their sum is proportional to the coefficient μ. For fixed μ, an elevated coefficient n_{NL} increases μ_Λ in (50). This causes a weakening of the breaking wave effect in (61) and a decrease of Λ in (62) for $B < B_{sat}$, where the breaking wave influence is already relatively small. Lowering the value of n_{NL}, on the other hand, leads to a relative increase in Λ and the breaking wave effect for $B < B_{sat}$. For $B \to B_{sat}$ the balance (64) can be dominated by dissipation and input to breaking waves, so that nonlinear interactions are negligible. For $n_{NL} \to 1$ (nonlinear interactions completely balance the wind-input), results are nearly unaltered compared to the results obtained for $n_{NL} = 0$, except that the breaking distribution approaches zero where $B < B_{sat}$. Similarly, $n_{NL} = -1$ (nonlinear interactions provide as much energy input as the wind-input) alters Λ only at low k, where Λ increases approximately by a factor of two. Results for the Charnock coefficient are nearly independent of n_{NL} (changes less than 1%).

4 Summary and conclusions

We have developed a coupled wave and wind model that incorporates the enhanced form drag of breaking waves. Combining the approaches by Hara and Belcher (2002,2004) and KHB,

the model is based on wave energy conservation and energy and momentum conservation in the wave boundary layer. These conservation principles lead to a system of coupled nonlinear advance-delay differential equations governing the wind speed, turbulent wind stress, wave height spectrum, and breaking wave distribution. To close the system of equations, we introduce a relationship between the wave height spectrum and the breaking wave distribution. For low values of B, this relationship is based on four-wave nonlinear interactions being proportional to dissipation (*Phillips*, 1985). As B increases beyond a threshold, the wave height spectrum is dissipation limited (*Phillips*, 1958).

The system of equations has been solved numerically for mature seas with wave ages greater than 20 (*Drennan et al.*, 2003), where the wind forcing is only significant for shorter waves away from the spectral peak (in the equilibrium range). Our model predicts a transition of the saturation spectrum from $k^{1/2}$ to k^0 at higher wavenumbers, and thus reconciles the two asymptotic limits of Phillips (1985) and Phillips (1958). The directional spreading changes from a cosine distribution relatively close to the spectral peak to an omnidirectional distribution at higher wavenumbers. The effect of breaking waves on the wave height spectrum is weak. The relationship between the one-dimensional breaking distribution and wave scale (expressed in k or c) depends on the particular set of parameters. Generally, Λ as function of c is approximately proportional to c^{-6} for longer waves and proportional to c^{-5} for intermediate scale waves.

Finally, we have estimated the sensitivity of the Charnock coefficients (normalized roughness length) on wave parameters for mature seas. Based on model results, it is likely that breaking waves support roughly 6 to 75% of the total wave form drag depending on the wave field. Therefore, to accurately model air-sea momentum fluxes, one must account for the enhanced from drag of breaking waves. Both the total momentum flux (drag coefficient) and the stress partitioning depend sensitively on the representation of the wave height spectrum. Hence, understanding systematically the dependence of wave spectra on wind speed and sea state is critical to improve predictions of the total wind stress over the ocean surface. In Part 2 we will apply our model to a wide range of wind and wave conditions.

Acknowledgements

We would like to thank two anonymous reviewers for their helpful comments and suggestions, which improved the manuscript. This work was supported by the U.S. National Science Foundation (Grant OCE- 0526177) and the U.S. Office of Naval Research (Grant N00014-06-10729).

A Numeric solutions

In order to solve the system (54) to (60) on the interval $[K_0, K_1]$ (corresponding to waves with wavenumbers between k_0 and k_1 and heights between ϵ/k_1 and ϵ/k_0), we first choose a grid of N points x_j on $[K_0, K_1]$, where $j = 1...N$, $x_1 = K_0$ and $x_N = K_1$. Next we approximate the solution S, U, and S_w by $(N-1)$ cubic polynomials S_j, U_j, and S_{wj}, which interpolate the solution and its first derivative at both ends of the interval $[x_j, x_{j+1}]$. Since the solution is estimated globally, the advance delay terms can be calculated explicitly. The polynomials are expressed as their Hermite presentation, so that for each x_j there are six coefficients that approximate the solution S, U, S_w and its derivative (see, e.g., *Shampine et al.* (2000)).

To determine the $6 \times N$ coefficients, we specify the three boundary conditions for S, U, S_w and impose that the approximate solution satisfies (54) to (64) at each x_j and midpoint of $[x_j, x_{j+1}]$ ("collocation equations"). The system of $6 \times N - 3$ non-linear algebraic equations is solved numerically using a damped, modified Newton's method (*Ascher et al.*, 1988). The grid spacing is determined empirically, so that solutions are sufficiently accurate and converging, typically $(x_{j+1} - x_j)$ is set to 0.2. K_1 is gradually increased until the solution becomes independent of the upper boundary condition.

For mature seas the longest forced wave is at $k_0 = g/u_*^2(0.07)^2$ (*Plant*, 1982), so that $S_0 = (0.07)^2$. Furthermore, $S_w(K_0) = 0$, since no waves with $k < k_0$ are forced. The delay terms in (58) and (60) vanishes for $K < K_0$, so that for K between $K_0 - \Delta$ and K_0 there is no input to non-breaking waves. The wind speed close to the surface is set to zero at $K_1 - \Delta$. Therefore, there is no input to breaking waves at heights corresponding to K between $K_1 - \Delta$ and K_1, so that the advance term in (61) to (64) vanish.

B Effect of breaking waves close to the spectral peak

Based on a scaling argument, one can show that for fully developed seas the energy input to breaking waves close to the lower wavenumber limit k_0 is small relative to wave dissipation. The maximum input (at $\theta = 0$) to breaking waves normalized by the wave energy loss is

$$\frac{I_b}{D} = \gamma^2 \ (u/c - 1)^2. \tag{72}$$

Evaluation of this expression close to $k = k_0$, where $\tau_t(k_0) \approx \tau_0$, results in

$$\left[\frac{I_b}{D}\right]_{k_0} = \gamma^2 \ \left(\frac{u}{u_*}\sqrt{S_0} - 1\right)^2. \tag{73}$$

An upper bound for the input to breaking waves is given by an upper bound of the wind speed, $u_{\max}$, i.e.,

$$\left[\frac{I_b}{D}\right]_{k_0} \leq \gamma^2 \ \left(\frac{u_{\max}}{u_*}\sigma_0^{-1} - 1\right)^2. \tag{74}$$

The maximum wind speed can be estimated by a lower limit of the Charnock coefficient, say $r_0 \approx 0.008$, so that $u_{\max} = \frac{u_*}{\kappa} \ln \frac{\epsilon g}{k_0 u_*^2 r_0}$. Substitution of this results in

$$\left[\frac{I_b}{D}\right]_{k_0} \leq \gamma^2 S_0 \left[\frac{1}{\kappa} \ln \frac{\epsilon}{r_0} - \frac{1}{\kappa} \ln S_0 - S_0^{-1/2}\right]^2. \tag{75}$$

With $S_0 = (0.07)^2$ and $\epsilon = 0.3$ the right hand side of the inequality is about 0.1% and 6% for $\gamma = 0.07$ (default value) and $\gamma = 0.5$ (upper bound), respectively. Therefore, the wind input to breaking waves close to the spectral peak is not a dominant term in the wave energy balance. Notice also that the upper limit increases with decreasing wave age until it approaches one, suggesting that the input to breaking waves close to the dominant wave may increase for younger seas.

C Approximation of the saturation spectrum and estimates of μ and B_{sat}

In Appendix B we have shown that the input to breaking waves is negligible near the lower wavenumber bound k_0. Since the turbulent stress is not significantly reduced for waves near

k_0 (see Figures 7 to 9), the wave spectrum can be approximated from (31) [with $h_\beta = \cos^2\theta$ and μ defined in (47)]. For $\mu c_\beta^{-1}\frac{u_*}{c}\cos\theta < B_{sat}$

$$B(k,\theta) = \mu c_\beta^{-1}\frac{u_*}{c}\cos\theta \tag{76}$$

On the other hand, once the saturation spectrum approaches B_{sat},

$$B(k,\theta) = B_{sat}. \tag{77}$$

Figure 1 shows that the combination of these two approximations is close to the solution of the full model.

The coefficients μ and B_{sat} are adjusted to be consistent with previous observations of the wave spectrum.

C.1 μ

Phillips (1985) introduces a parameterization of the saturation spectrum

$$B(k,\theta) = \frac{\alpha_p}{4} g^{-1/2} u_* k^{1/2}\cos\theta. \tag{78}$$

Comparing this equation to (76), his coefficient α_p is related to our model coefficient μ such that

$$\alpha_p = \frac{4\mu}{c_\beta}. \tag{79}$$

C.2 B_{sat}

Our model result suggests that $B(k,\theta)$ will converge to B_{sat} for high k. Therefore, we will match B_{sat} to observations of $B \approx$ constant. Banner et al. (1989) measured wavenumber spectra of short gravity waves ($\lambda = 0.2 - 1.6$m or $k = 4 - 31\text{m}^{-1}$), using stereophotography. They found $B(k,\theta) \approx 0.0012$. Banner et al. estimate the spectrum for all angles between 0 and 360°. Note that there is a 180° ambiguity for Fourier transforms on stationary images. Since in our theory waves cannot propagate against the wind direction, we take $B_{sat} \approx 0.0024$.

More recently, Melville and Matusov (2002) measured the wavenumber spectrum along a flight track in upwind and downwind directions for waves between $k = 0.1 - 3\mathrm{m}^{-1}$,

$$\begin{aligned} \Psi_x(k_x) &= \int_{-\infty}^{\infty} \Psi(k_x, k_y) dk_y \\ &= \int_{-\infty}^{\infty} B(k) k^{-4} h(k, \theta) dk_y, \end{aligned} \tag{80}$$

where Ψ_x denotes the marginal spectrum and $k = \sqrt{k_x^2 + k_y^2}$, and $\theta = \arctan(\frac{k_y}{k_x})$. In the high k limit, one may approximate the marginal spectrum from our solution by

$$\begin{aligned} \Psi_x(k_x) &= \int_{-\infty}^{\infty} B_{sat} k^{-4} dk_y \\ &= B_{sat} \int_{-\infty}^{\infty} \left(k_x^2 + k_y^2\right)^{-2} dk_y \\ &= \frac{\pi}{2} B_{sat}\ k_x^{-3}. \end{aligned} \tag{81}$$

From Melville and Matusov (2002) spectrum, we find for $k > 0.4\mathrm{m}^{-1}$, $k_x^3 \Psi_x = (1.6 \pm 0.4) \times 10^{-3}$, which results in $B_{sat} = (1.0 \pm 0.3) \times 10^{-3}$. Note that if the angular spreading is not omnidirectional, the estimate for B_{sat} will increase. For example, for $B(k, \theta) = B_{sat} \cos^2 \theta$, $B_{sat} = (1.4 \pm 0.4) \times 10^{-3}$. Also, B_{sat} might be underestimated if the wavenumber range is too close to the spectral peak, so that $B(k)$ still increases with k (as found by Melville and Matusov for $k > 20/\mathrm{m}$). If frequency spectra in the saturation range are converted to wavenumber spectra via the dispersion relation, $B(k)$ is approximately $B(k) \approx 0.006$ (*Phillips*, 1977). Assuming an omnidirectional spreading function, B_{sat} results in $B_{sat} \approx 0.002$. *Banner et al.* (2002) found a threshold for the saturation spectrum in the frequency range $\omega/\omega_p = 1 - 2.48$, above which the breaking probability significantly increases. Their data suggest that $B(k)$ does not exceed 0.006, corresponding roughly to $B(k, \theta) < 0.002$. In summary, observations indicate that B_{sat} likely is between 0.001 and 0.003. However, since B_{sat} was also inferred from one-dimensional spectra and since an assumed angular distribution that peaks in the wind direction increases B_{sat} relative to the omnidirectional distribution, we assume a generous upper bound of $B_{sat,\max} = 0.005$.

References

Alves, J. H. G. M., and M. L. Banner (2003), Performance of a saturation-based dissipation-rate source term in modeling the fetch-limited evolution of wind waves, *J. Phys. Oceanogr.*, *33*, 1274–1298.

Ascher, U. M., R. M. Mattheij, and R. D. Russell (1988), *Numerical solutions of boundary value problems for ordinary differential equations*, 1st ed., 595 pp., Prentice Hall, New Jersey, USA.

Banner, M. L. (1990), The influence of wave breaking on the surface pressure distribution in wind-wave interactions, *J. Fluid Mech.*, *211*, 463–495.

Banner, M. L., and D. H. Peregrine (1993), Wave breaking in deep water, *Annu. Rev. Fluid Mech.*, *25*, 373–397.

Banner, M. L., I. S. F. Jones, and J. C. Trinder (1989), Wavenumber spectra of short gravity waves, *J. Fluid Mech.*, *198*, 321–344, doi:10.1017/S0022112089000157.

Banner, M. L., J. R. Gemmrich, and D. M. Farmer (2002), Multiscale measurements of ocean wave breaking probability, *J. Phys. Oceanogr.*, *32*, 3364–3375.

Belcher, S. E. (1999), Wave growth by non-separated sheltering, *18*, 447–462.

Belcher, S. E., and J. C. R. Hunt (1993), Turbulent shear flow over slowly moving waves, *J. Fluid Mech.*, *251*, 109–148.

Belcher, S. E., and J. C. R. Hunt (1998), Turbulent flow over hills and waves, *Annu. Rev. Fluid Mech.*, *30*, 507–538.

Belcher, S. E., and J. C. Vassilicos (1997), Breaking waves and the equilibrium range of wind-wave spectra, *J. Fluid Mech.*, *342*, 377 – 401.

Cavaleri, L. (2006), Wave modeling, where to go in the future, *Bull. Amer. Meteorol. Soc.*, *87*(2), 207–214.

Chalikov, D. V., and V. K. Makin (1991), Models of the wave boundary layer, *Boundary Layer Meteorol.*, *56*, 83–99.

Cohen, I. M., and P. K. Kundu (2002), *Fluid dynamics*, 2nd ed., 730 pp., Academic Press, San Diego, Calif.

Drennan, W. M., H. C. Graber, D. Hauser, and C. Quentin (2003), On the wave age dependence of wind stress over pure wind seas, *J. Geophys. Res.*, *108*(C3), 8062, doi: 10.1029/2000JC000715.

Hara, T., and S. E. Belcher (2002), Wind forcing in the equilibrium range of wind-wave spectra, *J. Fluid Mech.*, *470*, 223–245.

Hara, T., and S. E. Belcher (2004), Wind profile and drag coefficient over mature ocean surface wave spectra, *J. Phys. Oceanogr.*, *34*, 2345–2358.

Hwang, P. A., D. W. Wang, E. J. Walsh, W. B. Krabill, and R. N. Swift (2000a), Airborne measurements of the wavenumber spectra of ocean surface waves. Part I: Spectral slope and dimensionless spectral coefficient, *J. Phys. Oceanogr.*, *30*(11), 2753–2767.

Hwang, P. A., D. W. Wang, E. J. Walsh, W. B. Krabill, and R. N. Swift (2000b), Airborne measurements of the wavenumber spectra of ocean surface waves. Part II: Directional distribution, *J. Phys. Oceanogr.*, *30*(11), 2768–2787.

Janssen, P. A. E. M. (1982), Quasilinear approximation for the spectrum of wind-generated waves, *J. Fluid Mech.*, *117*, 493–506.

Janssen, P. A. E. M. (1989), Wave-induced stress and the drag of air flow over sea waves, *J. Phys. Oceanogr.*, *19*(6), 745–754.

Jenkins, A. D. (1992), A quasi-linear eddy-viscosity model for the flux of energy and momentum to wind waves using conservation-law equations in a curvilinear coordinate system, *J. Phys. Oceanogr.*, *22*(8), 843–858.

Jenkins, A. D. (1993), A simplified quasi-linear model for wave generation and airsea momentum flux, *J. Phys. Oceanogr.*, *23*(9), 2001–2018.

Johnson, H. K., J. H. H. J. Vested, and S. E. Larsen (1998), On the dependence of sea surface roughness on wind waves, *J. Phys. Oceanogr.*, *28*, 1702–1716.

Jones, I. S. F., and Y. Toba (Eds.) (2001), *Wind stress over the ocean*, 1st ed., 307 pp., Cambridge Univ. Press, Cambridge, Great Britain.

Kitaigorodskii, S. A. (1983), On the theory of the equilibrium range in the spectrum of wind-generated gravity waves, *J. Phys. Oceanogr.*, *13*, 816–827.

Komen, G. J., L. Cavaleri, M. Donelan, K. Hasselmann, S. Hasselmann, and P. A. E. M. Janssen (Eds.) (1996), *Dynamics and modelling of ocean waves*, 1st ed., 532 pp., Cambridge Univ. Press, Cambridge, Great Britain.

Kudryavtsev, V. N., and V. K. Makin (2001), The impact of air-flow separation on the drag of the sea surface, *Boundary Layer Meteorol.*, *98*, 155–171.

Kukulka, T. (2006), The effect of breaking waves on a coupled model of wind and ocean surface waves, PhD Thesis, Univ. Rhode Island, 183 pp.

Kukulka, T., and H. Hara (2005), Momentum flux budget analysis of wind-driven air-water interfaces, *J. Geophys. Res.*, *110*, C12020, doi:10.1029/2004JC002844.

Kukulka, T., and H. Hara (2007), The effect of breaking waves on a coupled model of wind and ocean surface waves: II. Growing seas, submitted to *Journal of Physical Oceanography.*

Kukulka, T., T. Hara, and S. Belcher (2007), A model of the airsea momentum flux and breaking-wave distribution for strongly forced wind waves, *J. Phys. Oceanogr.*, *37*(7), 1811–1828.

Makin, V. K., and V. N. Kudryavtsev (1999), Coupled sea surface-atmosphere model 1. Wind over waves coupling, *J. Geophys. Res.*, *104*(C4), 7613–7624.

Makin, V. K., and C. Mastenbroek (1996), Impact of waves on air-sea exchange of sensible heat and momentum, *Boundary Layer Meteorol.*, *79*, 279–300.

Makin, V. K., V. N. Kudryavtsev, and C. Mastenbroek (1995), Drag of the sea surface, *Boundary Layer Meteorol.*, *73*, 159–182.

Melville, W. K. (1996), The role of surface-wave breaking in air-sea interaction, *Annu. Rev. Fluid Mech.*, *28*, 279–321.

Melville, W. K., and P. Matusov (2002), Distribution of breaking waves at the ocean surface, *Nature*, *417*, 58 – 63, doi:10.1038/417058a.

Phillips, O. (1958), The equilibrium range in the spectrum of wind-generated waves, *J. Fluid Mech.*, *4*, 426–434.

Phillips, O. (1977), *The Dynamics of the Upper Ocean*, 2nd ed., 336 pp., Cambridge Univ. Press, Cambridge, Great Britain.

Phillips, O. (1985), Spectral and statistical properties of the equilibrium range in wind-generated gravity waves, *J. Fluid Mech.*, *156*, 505 – 531.

Plant, W. J. (1982), A relationship between wind stress and wave slope, *J. Geophys. Res.*, *87*(C3), 1961–1967.

Shampine, L. F., J. Kierzenka, and M. W. Reichelt (2000), Solving boundary value problems for ordinary differential equations in Matlab with bvp4c, http://www.mathworks.com/support/solutions/files/s8314/bvp_paper.pdf (accessed 12/2006).

Smith, S. D., et al. (1992), Sea surface wind stress and drag coefficients: The HEXOS results, *Boundary Layer Meteorol.*, *60*, 109–142.

List of Figures

Tables

B_{sat}	μ	$\tau_w/\tau_0(\%)$	$\tau_b/\tau_0(\%)$	r	$r(\gamma=0)$
0.001	0.125	25	75	0.009	<0.001
0.001	0.6	29	71	0.009	<0.001
0.001	0.813	29	71	0.009	<0.001
0.002	0.125	42	58	0.011	0.002
0.002	0.6	55	45	0.015	0.004
0.002	0.813	56	44	0.015	0.004
0.005	0.125	69	31	0.015	0.006
0.005	0.6	92	8	0.037	0.030
0.005	0.813	94	6	0.041	0.036
∞	0.125	83	17	0.019	0.011
∞	0.6	99	1	0.076	0.074
∞	0.813	100	0	0.093	0.093

Table 1: Charnock coefficient r for smallest, default, and greatest values of B_{sat} and μ. Other parameters are $c_\beta = 25, \gamma = 0.07, \delta = 0.05, \epsilon = 0.3$. The stress partitioning between breaking and non-breaking waves is calculated under the assumption that the total stress is supported by the wave form drag (high wind conditions). The last column shows the results without wind input to breaking waves ($\gamma = 0$).

Figures

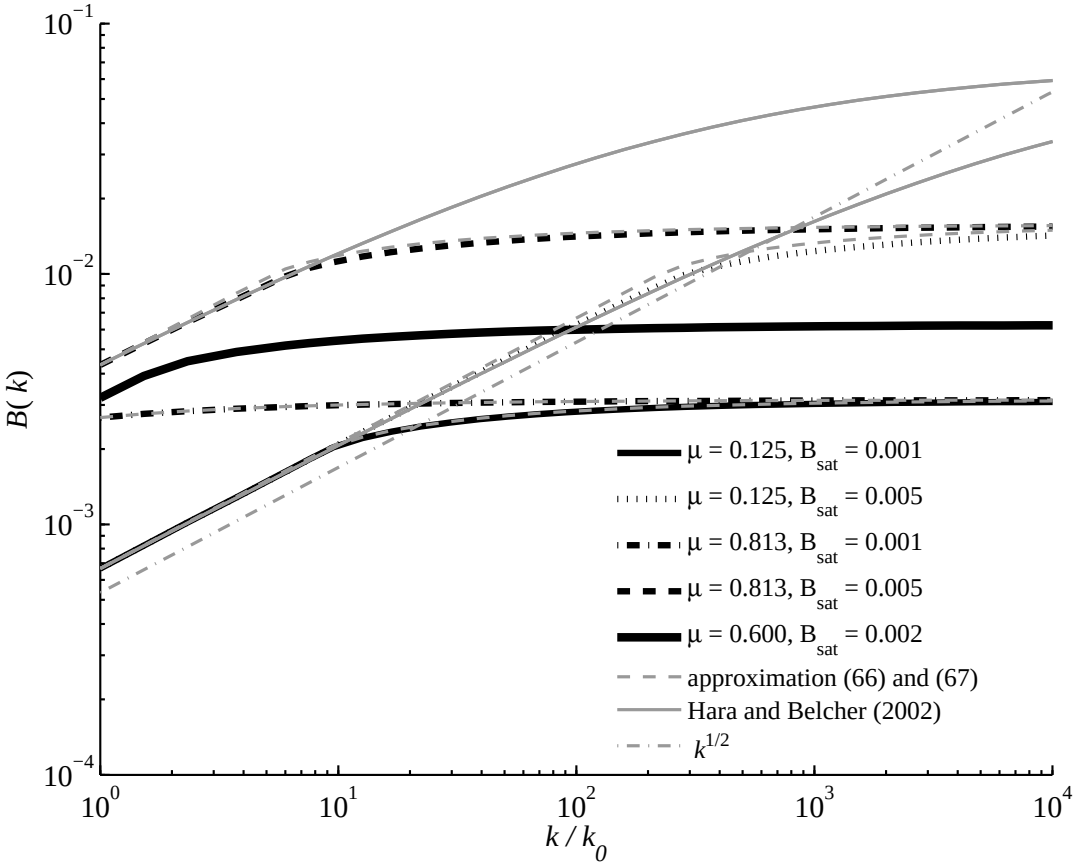

Figure 1: One-dimensional saturation spectrum $B(k)$ as a function of k/k_0. Black lines are solutions for different μ and B_{sat}. Grey lines are asymptotic solutions.

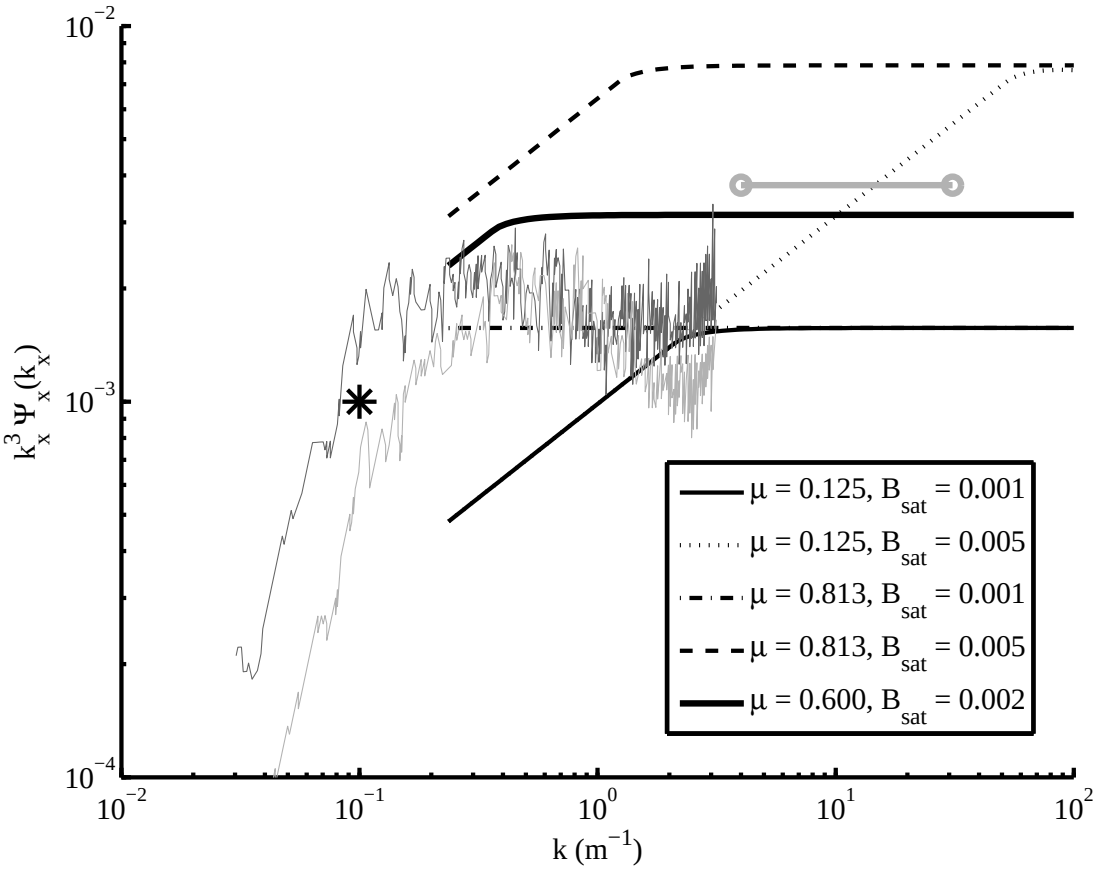

Figure 2: Comparison of model result for marginal saturation spectrum at $U_{10} = 10\text{ms}^{-1}$ with observations. Black lines are model results for different μ and B_{sat} (compare Figure 1), previous observations from Melville and Matusov (2002) for $U_{10} = 13.6\text{ms}^{-1}$ (dark gray thin line) and 9.8 ms^{-1} (light gray thin line), from Hwang (2000a) for $U_{10} = 5.5 - 9.5\text{ms}^{-1}$ (star), and from Banner et al. (1989) for $U_{10} = 5.5 - 13.3\text{ms}^{-1}$ (thick gray line, end points circles).

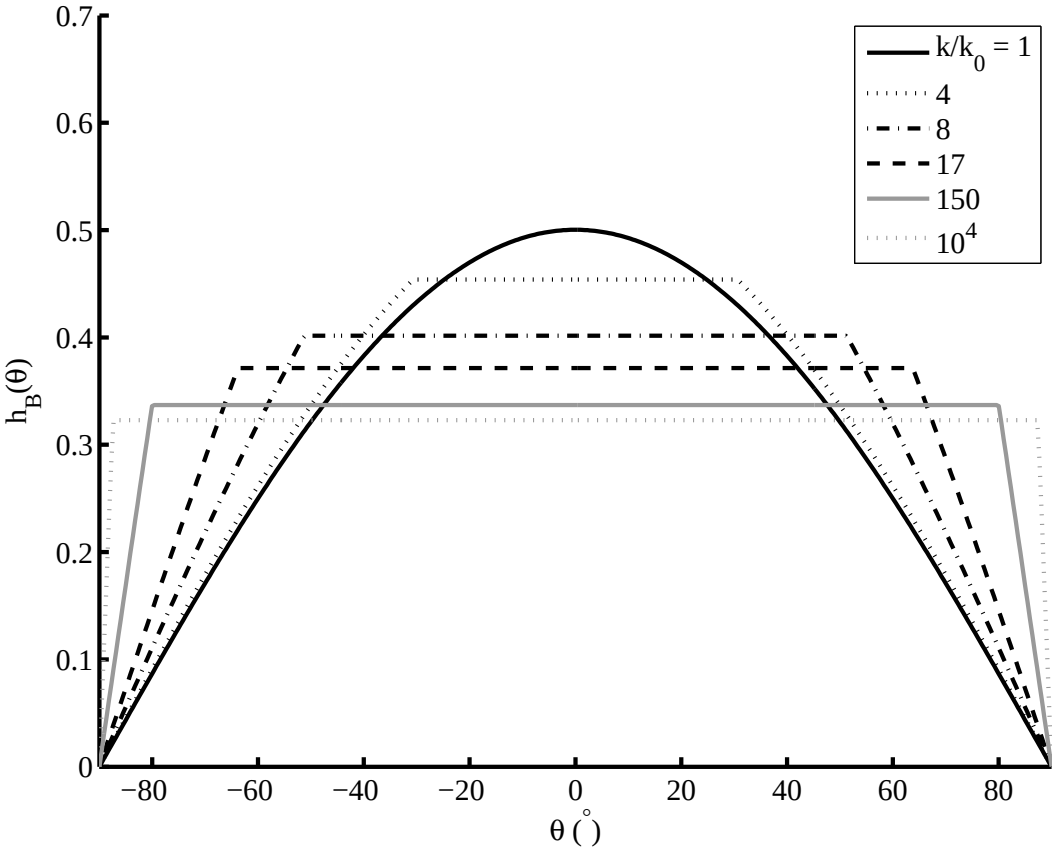

Figure 3: Directionality of the modeled saturation spectrum for $B_{sat} = 0.002$ and $\mu = 0.6$.

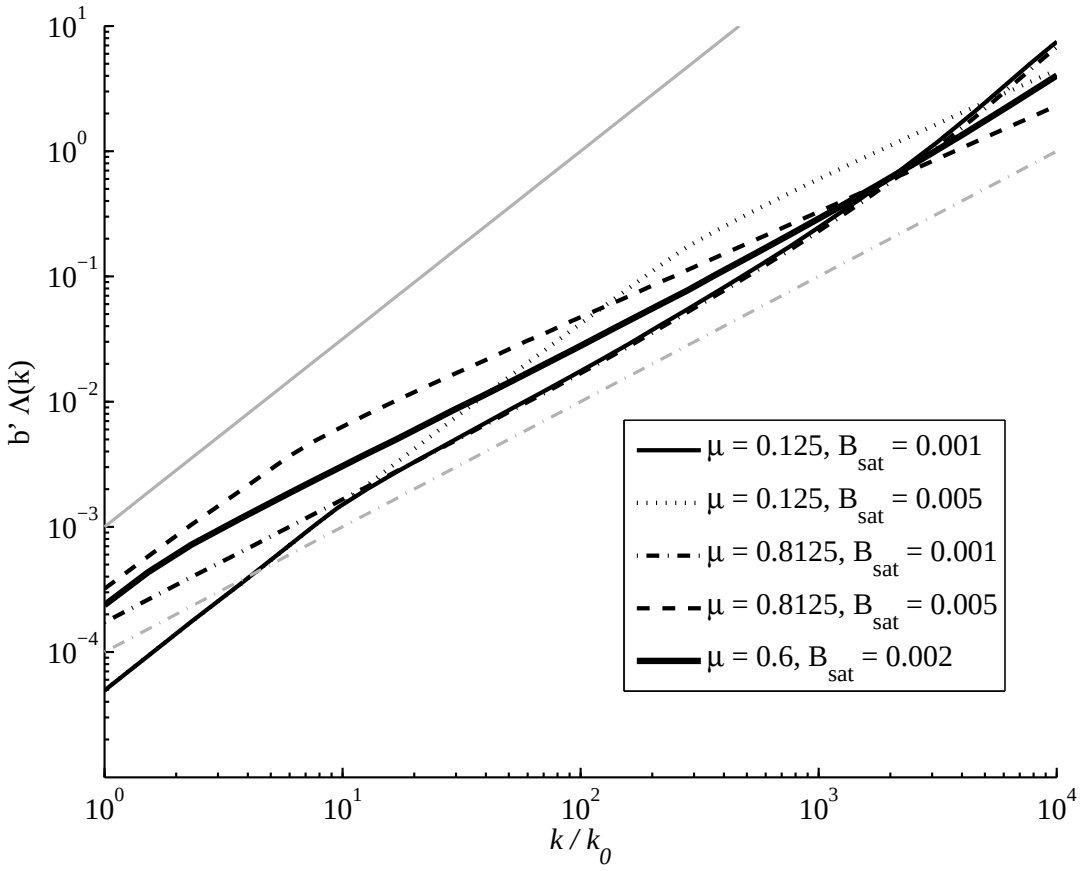

Figure 4: One-dimensional breaking wave distribution $b'\Lambda(k)$ for different μ and B_{sat}; $k^{3/2}$ (gray solid line), k (gray dash-dotted line).

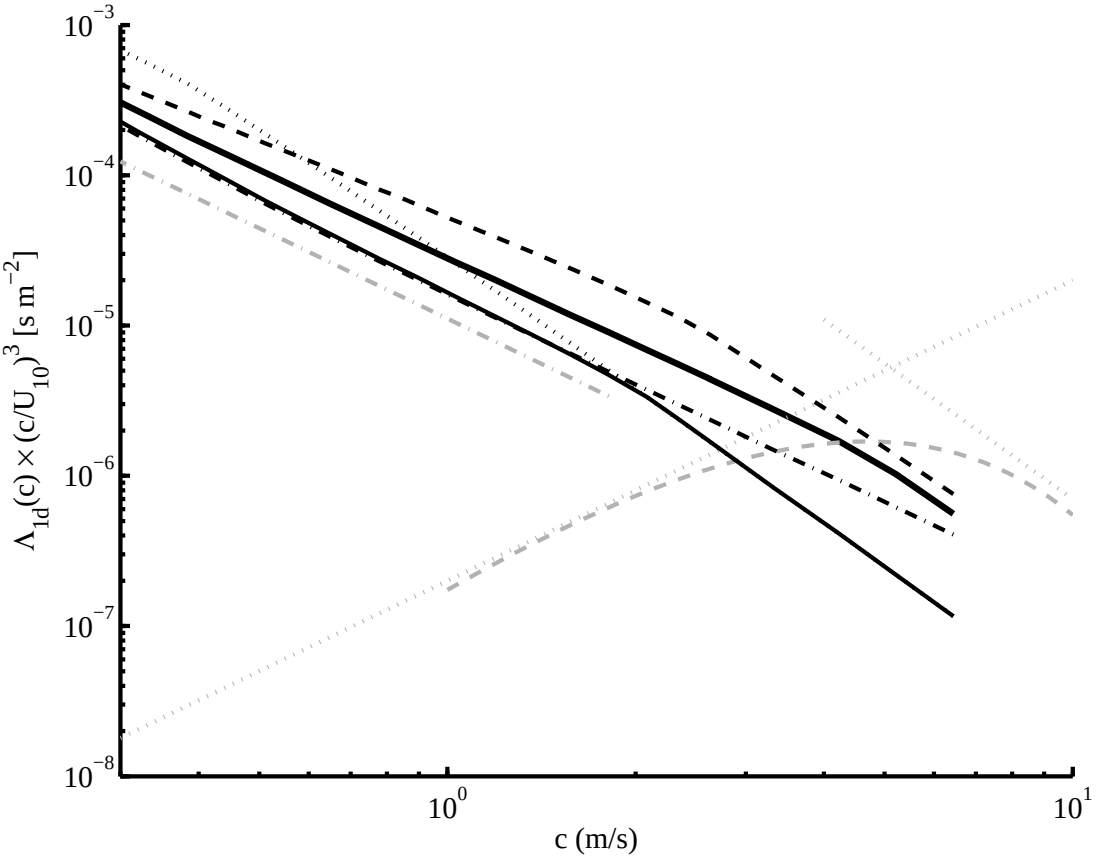

Figure 5: Comparison of modeled normalized breaking wave distribution $c^3 U_{10}^{-3} \Lambda(c)$ at $U_{10} = 10\text{ms}^{-1}$ with observations. Model results for different μ and B_{sat} (black lines, line style as in Figure 4); best exponential fits from Melville and Matusov (2002) based on observations (gray dashed line), power law fits $\Lambda(c) \propto c^{-1}$ and $\Lambda(c) \propto c^{-6}$ for low and high phase speeds (gray dotted lines); arbitrary c^{-2} line corresponding to $\Lambda(c) \propto c^{-5}$ (gray dash-dotted line).

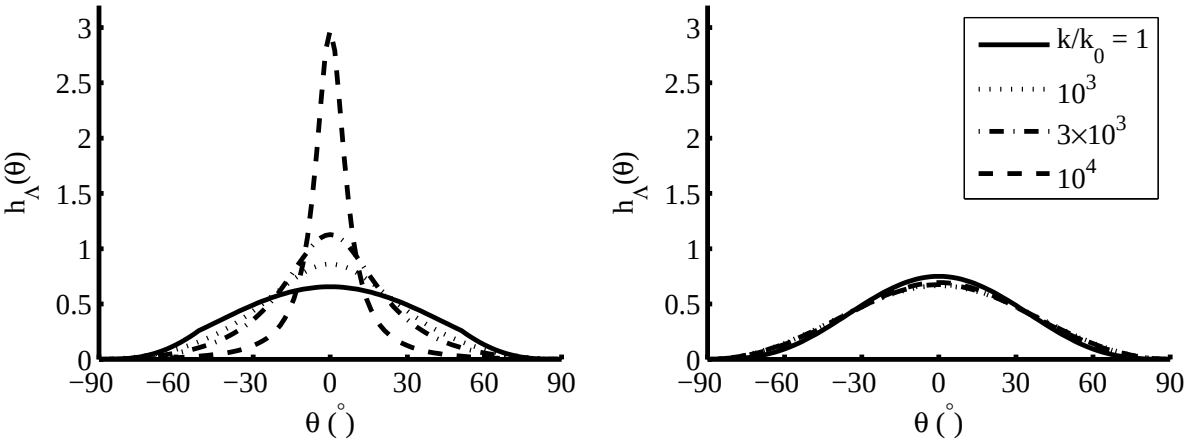

Figure 6: Modeled directionality of breaking wave distribution for $B_{sat} = 0.001$, $\mu = 0.6$ (left) and for $B_{sat} = 0.005$, $\mu = 0.6$ (right).

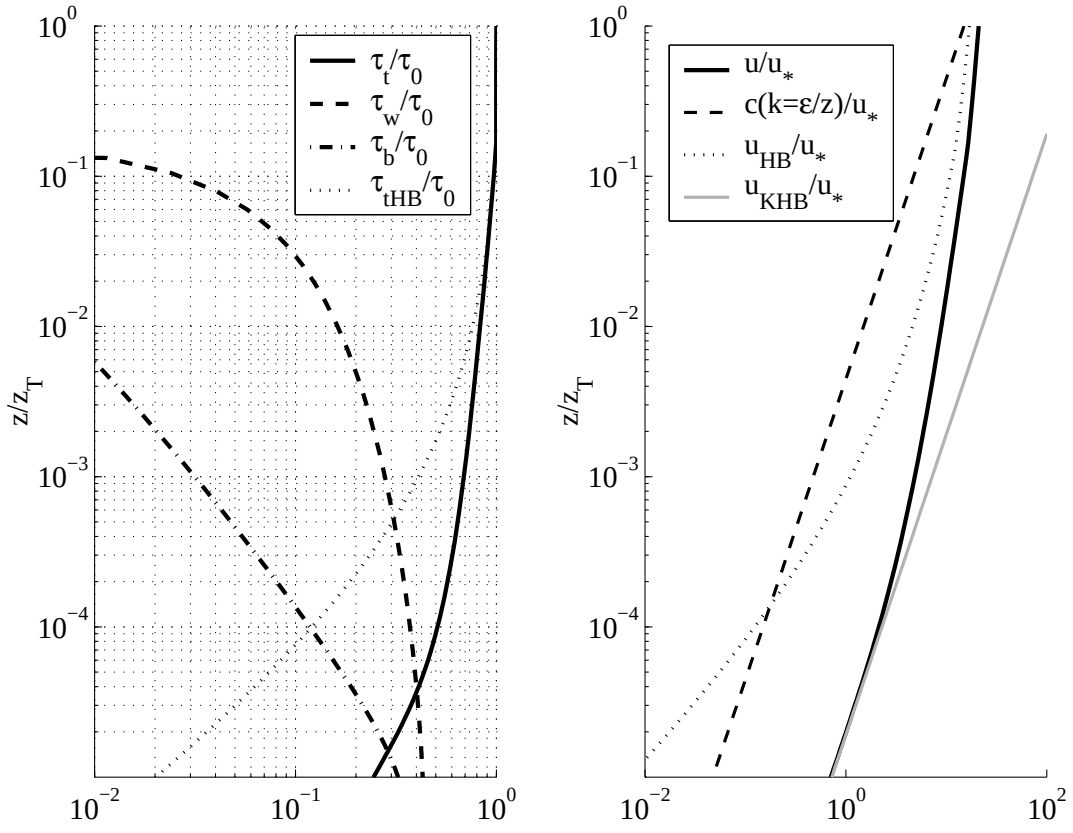

Figure 7: Modeled wind stress partitioning (left panel) and wind speed profile (right panel) for $\mu = 0.6$, $B_{sat} = 0.002$. Analytic solutions HB (*Hara and Belcher*, 2002, 2004), KHB (*Kukulka et al.*, 2007). The top of the wave boundary layer is at $z_T = \epsilon/k_0$.

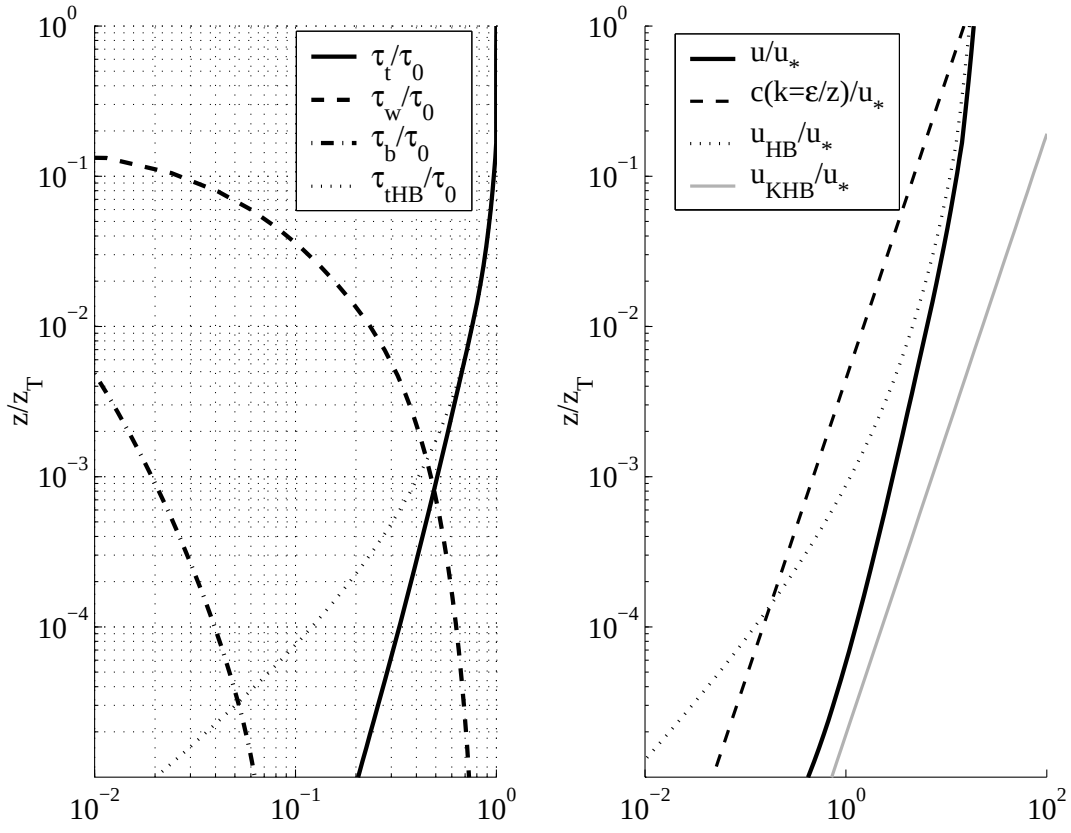

Figure 8: Same as Figure 7, except $B_{sat} = 0.005$ (non-breaking dominated).

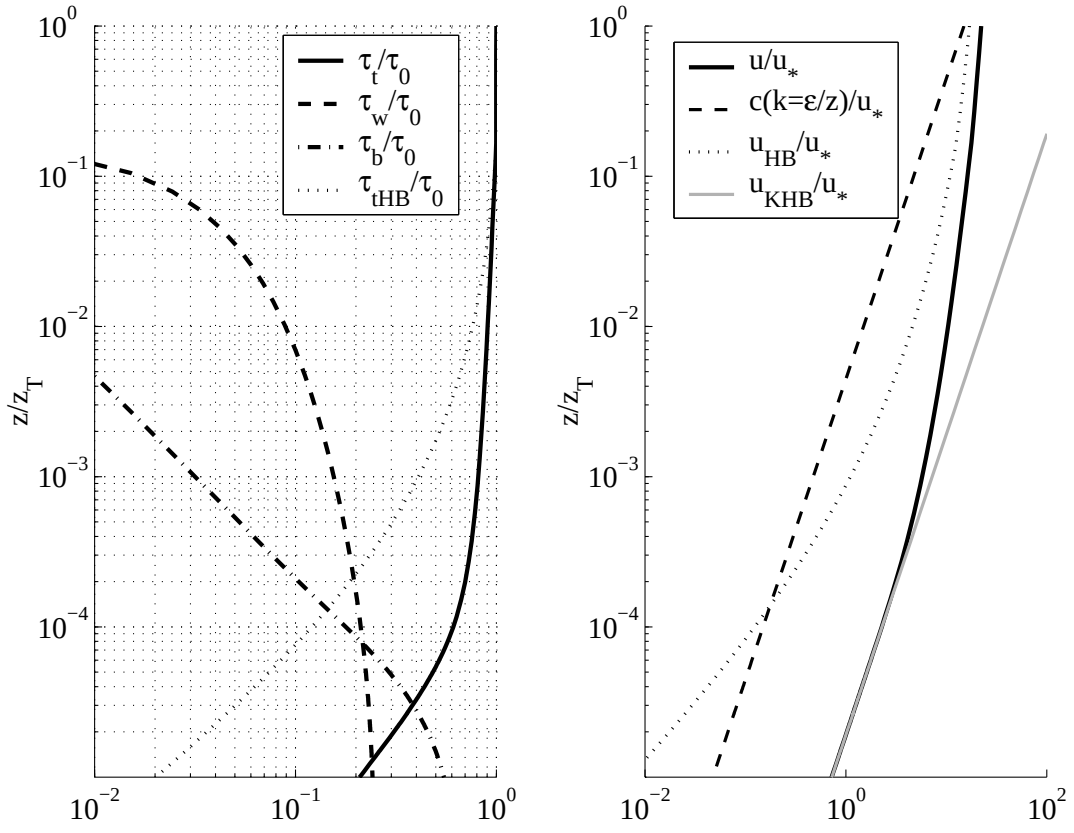

Figure 9: Same as Figure 7, except $B_{sat} = 0.001$ (breaking dominated).